buildings

MDPI

Article

Experimental and Finite Element Analysis of Reinforced Concrete Beams Using Ferronickel Slag as Partial Replacement for Fine Aggregate under Semi-Cyclic Loading

Jessica Sjah [1,*], Eristra Ernawan [1], Nuraziz Handika [1], Sotya Astutiningsih [2] and Eric Vincens [3]

[1] Department of Civil Engineering, Faculty of Engineering, Universitas Indonesia, Depok 16424, Indonesia
[2] Department of Metallurgical and Material Engineering, Faculty of Engineering, Universitas Indonesia, Depok 16424, Indonesia
[3] CNRS, ENTPE, LTDS, UMR5513, Ecole Centrale de Lyon, University Lyon, 69134 Ecully, France
* Correspondence: jessicasjah@ui.ac.id

Abstract: The smelting process of Ferronickel in Indonesia produces a significant amount of waste in the form of Ferronickel Slag (FNS), with an annual accumulation of up to 13 million metric tons. Previous studies have shown promising strength results for concrete utilizing FNS as a fine aggregate. This study aims to analyze the mechanical properties of three reinforced concrete (RC) beams measuring 15 cm × 25 cm × 300 cm, each containing FNS as a 50% substitute for fine aggregate. The RC Beams underwent experimental testing using a four-point loading scheme under semi-cyclic loading conditions. Test results show the beams' capacity had reached up to 8 ton-f and their load–displacement responses show promising results. Digital Image Correlation (DIC) analysis facilitated the observation of surface deformation evolution due to loading, aiding in the identification of concrete crack patterns. Due to semi-cyclic loading, cracks on the beams' surface were experiencing a crack opening and closing phenomenon, where the propagations of cracks ceased or reclosed throughout the unloading process. Moreover, the opening of residual cracks was also captured by DIC analysis. The experimental finding was validated by finite element analysis. The RC beam numerical model was created using the Timoshenko Multi-fiber element in CAST3M software version 2022. Mazars concrete and elastoplastic steel damage model were used as constitutive laws for numerical modeling. The model's load–displacement response demonstrated satisfactory agreement compared to the experimental monotonic loading result. However, the model had limitations regarding the simulation of residual displacements of beams due to semi-cyclic loading.

Keywords: Ferronickel Slag; digital image correlation (DIC); CAST3M; semi-cyclic loading; concrete structure

check for updates

Citation: Sjah, J.; Ernawan, E.; Handika, N.; Astutiningsih, S.; Vincens, E. Experimental and Finite Element Analysis of Reinforced Concrete Beams Using Ferronickel Slag as Partial Replacement for Fine Aggregate under Semi-Cyclic Loading. *Buildings* **2024**, *14*, 2151. https://doi.org/10.3390/buildings14072151

Academic Editor: Giuseppe Santarsiero

Received: 10 June 2024
Revised: 5 July 2024
Accepted: 9 July 2024
Published: 12 July 2024

Copyright: © 2024 by the authors. Licensee MDPI, Basel, Switzerland. This article is an open access article distributed under the terms and conditions of the Creative Commons Attribution (CC BY) license (https://creativecommons.org/licenses/by/4.0/).

1. Introduction

Concrete, comprising water, cement, fine aggregate, and coarse aggregate, is the most used composite construction material. Approximately 60–75% of concrete volume is occupied by coarse and fine aggregates [1], with fine aggregates constituting 35% of the concrete volume [2]. Fine aggregates play a crucial role in filling the voids between coarse aggregates, thereby achieving a dense packing condition of the total aggregates, which enhances concrete volume stability [1]. An increase in packing density reduces the number of voids and the amount of cement paste required, thereby lowering concrete production costs [1]. However, its extensive use may deplete natural material supplies, such as natural sand [3]. Various waste materials have been explored as substitutes for concrete components [4–9], particularly as replacements for fine aggregate [10–26], including by-products from the mining, metal, and mineral industries.

The high content of iron, silica, and aluminum oxide in copper slag makes it suitable for use as a partial replacement for fine aggregate in concrete mixes. It is recommended

to use copper slag as a fine aggregate replacement in concrete at variations between 40% and 50% by weight to achieve good strength and durability [10]. Using copper slag within this range yields compressive strength in concrete comparable to that of conventional concrete. However, replacing fine aggregate with copper slag above this range reduces the compressive strength of the concrete.

The use of blast furnace slag as a partial replacement for fine aggregate in self-compacting concrete (SCC) at compositions of 10%, 20%, 30%, 40%, 50%, and 60% was investigated [11]. The research indicates that, over the long term, SCC containing blast furnace slag achieves higher compressive strength compared to SCC without blast furnace slag. However, increasing the percentage of blast furnace slag as a partial replacement for fine aggregate in SCC increases porosity, reduces stiffness, and accelerates water loss.

Industrial waste materials, such as quarry dust, glass powder, ceramic dust, and coal dust, have been used as substitutes for fine aggregate in concrete [12]. Quarry dust, glass powder, and ceramic dust can effectively replace up to 20% of fine aggregate. However, the use of coal dust is unsuitable as a replacement for fine aggregate because it decreases the concrete's compressive strength. A cost analysis conducted for application in paving block concrete concluded that quarry dust, when used to replace 40% of fine aggregate, offers the most economic benefit among the tested waste materials.

The utilization of steel slag as a fine aggregate in concrete mixes with variations of 0%, 10%, 20%, 30%, and 40% was studied [13]. It was found that the optimal use of steel slag, specifically at a 20% replacement level, effectively enhances both the static and dynamic compressive strength of the concrete.

Surangi et al. [14] investigated the use of fly ash as a partial replacement for fine aggregate and cement in concrete. The study found that using fly ash as a partial replacement for fine aggregate resulted in higher compressive strength compared to its use as a partial replacement for cementitious material. The highest compressive strength was achieved with a 40% replacement of fine aggregate with fly ash. Additionally, concrete's resistance to carbonation was optimal with a 20% replacement of fine aggregate with fly ash.

There is substantial potential for development in utilizing Ferronickel Slag (FNS) as a construction material. The physical properties of FNS, a by-product of nickel ore smelting, closely resemble those of natural sand, making it a promising alternative fine aggregate for concrete [15,16]. Indonesia, as a major exporter of mining materials, has various vital mining commodities crucial for global industrial sustainability. According to the Mineral Commodity Summaries [27], Indonesia was the highest placed country in terms of nickel production worldwide in 2020, with an annual production capacity of 760 thousand tons and a nickel reserve capacity of 210 million tons. As a byproduct, 13 million tons of nickel slag is produced annually [28]. Proper processing and utilization are crucial to mitigate environmental impacts.

Several studies have investigated the use of FNS as a substitute for fine aggregate in concrete [15–26]. Wijaya [17] explored PCC mortar with FNS substitution, resulting in higher compressive strength and mortar density. Mustika et al. [19] studied OPC concrete with 33.3% FNS substitution, reporting improved workability but reduced compressive, tensile, and modulus of elasticity strengths. Edwin et al. [20] examined OPC concrete with FNS substitution, observing increased workability with FNS substitution. Additionally, concrete compressive strength increased up to 40% FNS content and decreased afterward.

Ernawan et al. [21] conducted a study on the mechanical properties of laboratory-scale concrete specimens using 15 cm × 15 cm × 15 cm cubes, with Ferronickel Slag (FNS) as a substitute for fine aggregate in the concrete mix. The proportions tested were 0%, 50%, and 100% FNS substitution. Manuel [22] built on research carried out by Ernawan et al. [21] by investigating additional proportions of 40% and 60% FNS substitution in concrete mixes. The variations in compressive strength test results with different FNS proportions are shown in Figure 1. This study indicated that the highest compressive strength was achieved with 50% FNS substitution. In addition to compressive strength, mechanical properties were evaluated using the Digital Image Correlation (DIC) method to assess

elasticity modulus, stiffness, and Poisson's ratio. Ernawan et al. [21] demonstrated that Ordinary Portland Cement (OPC) concrete with 50% FNS substitution exhibited improved homogeneity, compressive strength, and stiffness compared to normal concrete. The same conclusion was reported that the use of 50% FNS as a partial replacement for fine aggregate can enhance the compressive strength of concrete [23]. Another study found that using 50% FNS as a substitute for fine aggregate and 30% class F fly ash as a substitute for cement in concrete mixes could provide durability comparable to concrete without FNS and fly ash [24]. Moreover, the use of 50% FNS as a substitute for fine aggregate and 25% fly ash as a substitute for cement in concrete mixes has been proven to provide good resistance to alkali-silica reaction and chloride contamination [25]. Bao et al. [26] found that using 40–50% FNS as a substitute for fine aggregate in recycled concrete aggregates results in higher compressive strength and exhibits good resistance to chloride penetration and water absorption in concrete.

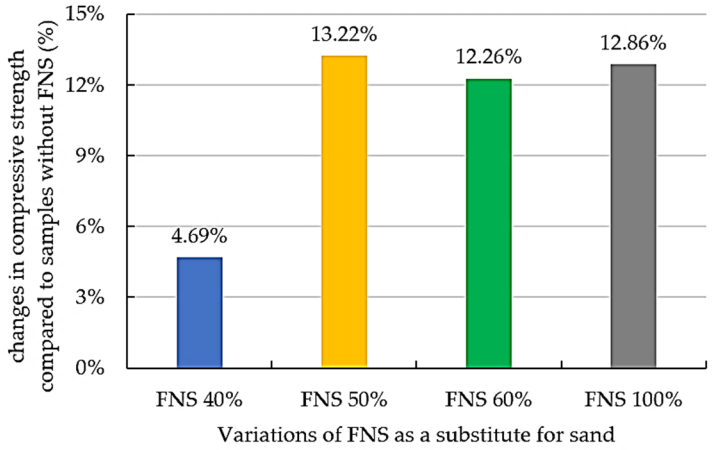


Figure 1. Changes in compressive strength due to variations of FNS as a substitute for sand compared to concrete samples without FNS.

There have been few studies that have evaluated the mechanical properties of reinforced concrete utilizing waste materials from industrial by-products under cyclic loading conditions. Such conditions are pertinent for applications involving high winds, ocean waves, and earthquakes, which are crucial considerations for offshore structures and high-rise buildings. Incorporating mineral materials into concrete can enhance ductility, energy dissipation, and seismic resilience in structural design [29].

Murad et al., (2019) [30] demonstrated that replacing cement with 15% pulverized fuel ash, silica fume, and iron filings enhances the performance of unconfined beam-column connections under cyclic loading. The study highlights the finding that using 15% pulverized fuel ash is particularly effective, offering structural benefits while reducing environmental impact. Ramasamy et al., (2022) [31] analyzed crack development using Ground Granulated Blast Furnace Slag (GGBFS) and steel fibers in high-performance concrete beams subjected to cyclic loading conditions. Raju et al. (2022) [29] investigated the substitution of fine aggregate with copper slag in reinforced concrete beams, ranging from 0% to 100% substitution. Their findings show that RC beams with 20% fly ash and 80% copper slag exhibit significantly higher ultimate load-carrying capacity, stiffness, and ductility compared to control beams, withstanding up to 18 loading cycles with an ultimate deflection of 60 mm.

There have been no studies reported on the use of FNS as a substitute for fine aggregate in reinforced concrete beams under semi-cyclic loading conditions. Furthermore, research on cyclic loading of reinforced concrete using waste materials typically involves experimental studies only. This study aims to further investigate the use of 50% FNS as a replacement for sand in concrete within real scale reinforced concrete beam structures under semi-cyclic loading conditions, employing both experimental and numerical approaches.

These findings are essential for guiding future applications of FNS in concrete construction and for advancing structural engineering practices toward more sustainable and resilient infrastructure solutions.

The focus in this study is on analyzing deformation characteristics due to semi-cyclic loading using four-point bending tests and the digital image correlation (DIC) method of reinforced concrete (RC) beams with a 50% FNS fine aggregate substitute. Three RC beam specimens measuring 15 cm × 25 cm × 300 cm were made and painted white with black speckles on one of its major faces. Digital images of the specimens were captured during the loading process and analyzed using GOM Correlate version 2022, a post-processing software for DIC. The outcomes of the experimental tests include the load–displacement relationship, strain analysis, evolution of surface deformation, and crack propagation. The experimental results will be validated by utilizing finite element analysis. The numerical model of reinforced concrete beams in CAST3M software version 2022 using multi-fiber Timoshenko elements with the Mazars concrete damage model will be performed and compared with the experimental results. Concrete's compressive and split-tensile properties were experimentally determined from cylinder samples to provide essential input parameters for the numerical simulations.

Utilizing Ferronickel Slag (FNS) as a 50% substitute for fine aggregate in reinforced concrete (RC) beams enhances their mechanical performance under semi-cyclic loading conditions, providing comparable or improved structural integrity and stiffness compared to conventional RC beams. Advanced experimental techniques, such as the Digital Image Correlation (DIC) method, effectively capture the material response, crack propagation, and load-deformation behavior. Numerical validation using the CAST3M model, incorporating Mazars concrete damage and elastoplastic steel models, showed reasonable agreement with experimental deflection data. These findings validate the feasibility of FNS as a sustainable alternative material for partial fine aggregate replacement in concrete construction.

2. Materials and Methods

2.1. Materials and Mix Proportions

This study used type I Ordinary Portland cement (OPC). Ferronickel Slag used as a substitute for fine aggregate was sourced from a Ferronickel smelter in Indonesia. This FNS, derived from nickel ore, is a by-product of the smelting and sorting process, during which it is cooled with water. This water-cooled slag solidifies into granules, and those with a size smaller than 0.5 mm were utilized in the experiment. The remaining fine aggregate was Manufactured sand (M-sand), sourced from Rumpin, Indonesia. M-sand is considered a more sustainable alternative to natural sand [32], as it is produced from crushed and granulated mining waste rock. Its particle size distribution is more uniform compared to river sand due to a regulated manufacturing process and reduced surface area, leading to improved concrete performance [33]. Coarse aggregates were sourced from Sudamanik, Indonesia, comprising split stones with a maximum nominal size of 25 mm.

The fine aggregate composition comprised 50% FNS and 50% M-sand, based on the total weight of the fine aggregate. This proportion was chosen based on optimal testing results from previous research by Ernawan et al. [21]. The properties of the fine aggregate with 50% FNS are presented in Table 1, with its particle size distribution shown in Figure 2. The particle size distribution of M-sand only (0% FNS) and FNS only (100% FNS) could be found in [21]. An X-ray fluorescence (XRF) test was conducted to determine the chemical composition of the FNS [21]. It was observed that the main components of the FNS are Silicon Oxide (46.91%), Magnesium Oxide (29.28%), Ferric Oxide (15.10%), and Aluminum Oxide (4.04%). This composition aligns closely with that of natural sand, primarily consisting of SiO_2. The specific gravity of FNS is 2.93 g/cm^3 [20]. The properties of the fine aggregate with 50% FNS substitution and the coarse aggregate are presented in Table 1. The concrete mix proportion by using 50% FNS as fine aggregates substitution from previous research was used as shown in Table 2. The magnitude of w/c ratio utilized was 0.412.

Table 1. Material properties of 50% FNS as fine aggregate and coarse aggregate [14].

Material Properties	Fine Aggregate with 50% FNS Substitution	Coarse Aggregate
Fineness Modulus (FM)	2.72	-
SSD Specific Gravity	2.76	2.58
Absorption (%)	1.42	1.60
Unit Weight	1.66	1.55
Void (%)	38.83	38.84
Finer than no. 200 sieve (%)	2.80	-
Abrasion Loss (%)	-	22.23

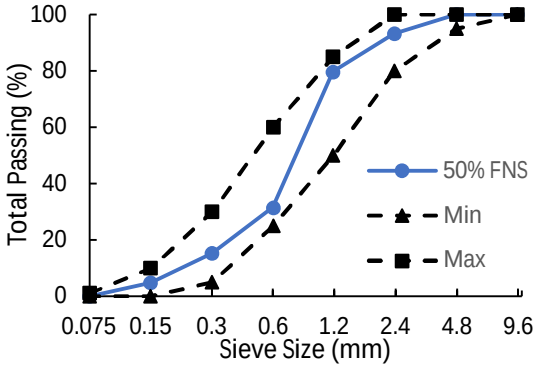


Figure 2. Particle size distribution of 50% FNS as fine aggregate.

Table 2. Mix proportion for 1 m^3 of concrete mixture [14].

Material	Magnitude (kg)
FNS	347
M-sand	347
Coarse Aggregate	992
Cement	501
Water	206

2.2. Beam Specimens

Three RC beams measuring 15 cm × 25 cm × 300 cm with 50% FNS fine aggregate were made and labeled as RC Beam 1, RC Beam 2, and RC Beam 3. Detailed information of the beams is shown in Table 3 and Figure 3. Additionally, cylindrical concrete specimens were prepared to provide compressive and split tensile strength data to be used later in the numerical model.

Table 3. Information of the RC beam specimens.

Component	Symbol	Value	Unit
Height	H	250	mm
Width	bw	150	mm
Length	L	3000	mm
Tension Rebar	D	13	mm
Compression Rebar	D	13	mm
Shear Rebar	Ø	6	mm
Main Rebar Grade	fy	420	MPa
Shear Rebar Grade	fyt	280	MPa
Concrete cover	ts	25	mm

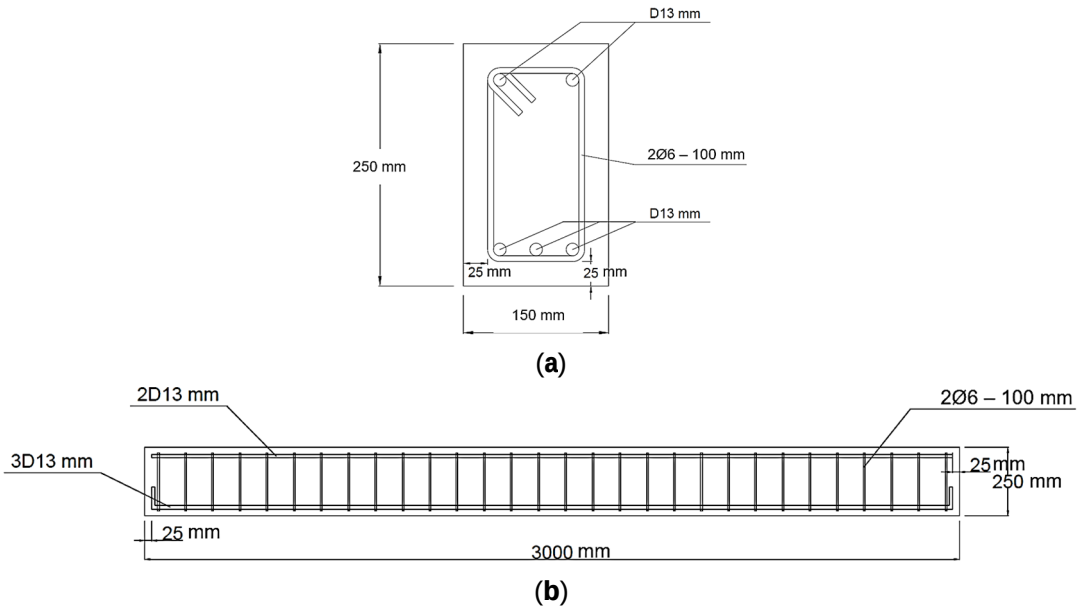


Figure 3. RC Beam specimens: (**a**) beam section, (**b**) beam dimension.

2.3. Experimental Methods

2.3.1. Compressive Strength

The concrete compressive strength is assessed using cylindrical specimens, each with a diameter of 15 cm and a height of 30 cm. Each of the three RC beam samples to be tested is accompanied by a set of three companion cylinder specimens. These companion cylinder specimens were tested at 28 days of age. The testing procedure for the concrete cylinders' compressive strength follows ASTM Standard C39/C39M [34]. The magnitude of compressive strength of companion specimens will be used in numerical model of RC beam in CAST3M.

2.3.2. Tensile Strength

The concrete tensile strength specimens are similar in form to the compressive strength specimens. There are three-cylinder specimens, each representing one of the three beam samples to be tested. The companion cylinder specimens are tested on the same day as the beams are subjected to flexural testing at 28 days of age. These companion specimens are intended to determine the tensile strength of the beams after casting. The tensile strength testing of concrete cylinders is performed according to ASTM Standard C496/C496M [35].

2.3.3. Fourth-Point Loading Test

The fourth-point loading on the RC beam specimens will be performed under semi-cyclic loading conditions. The RC beam specimens were tested at 28 days of age. The homogeneity of the RC beam specimens was evaluated using the ultrasonic pulse velocity test (UPV test). The UPV test for concrete were conducted in accordance with ASTM Standard C597 [36]. A direct method was utilized to measure the pulse's velocity propagated through the RC beam specimen, as shown in Figure 4.

There are several types of loading, consisting of monotonic loading, cyclic loading, and semi-cyclic loading. Monotonic loading involves continuously applying load in one direction until failure, assessing the ultimate strength and behavior of a concrete beam under a single, uninterrupted load. Cyclic loading, on the other hand, involves the repeated application of load in both directions with full reversals. In this research, the semi-cyclic loading condition will be used, which entails repeated loading with an unloading process, to study the structural response to repeated unidirectional loads.

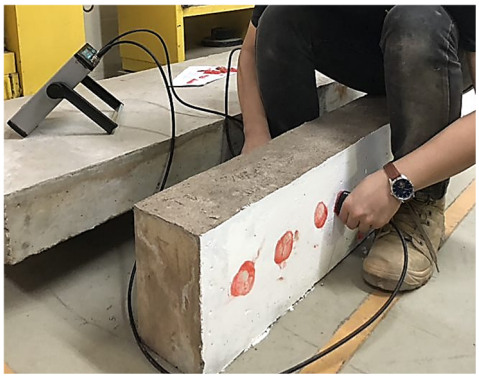


Figure 4. Homogeneity evaluation of RC beam specimen by UPV Test.

The beam loading scheme is presented in Figure 5. Loading for the samples will be conducted using a spreader beam equipped with a load cell connected to a hydraulic jack. Strain gauges, LVDTs, and load cells will be attached and connected to a computer. Loading will occur in cyclic patterns, with each cycle involving incremental load increases of 200 kg until reaching the maximum load. During Cycle 1, the sample will be subjected to a load of 2P until reaching 2 tons, followed by gradual load reduction in 200 kg increments until reaching 0. In cycles 2, 3, and 4, loads of 4 tons, 6 tons, and 8 tons, respectively, will be applied following the same procedure. Testing will continue until failure is observed in the reinforced beam samples. A semi-cyclic loading is performed through a cycle of loading and unloading, where the test specimen is loaded and then the load is released until reaching 0. Subsequently, the load is reapplied in the same direction. This is different from cyclic loading, where the load changes direction like a wave, creating a unique load–displacement relationship [37].

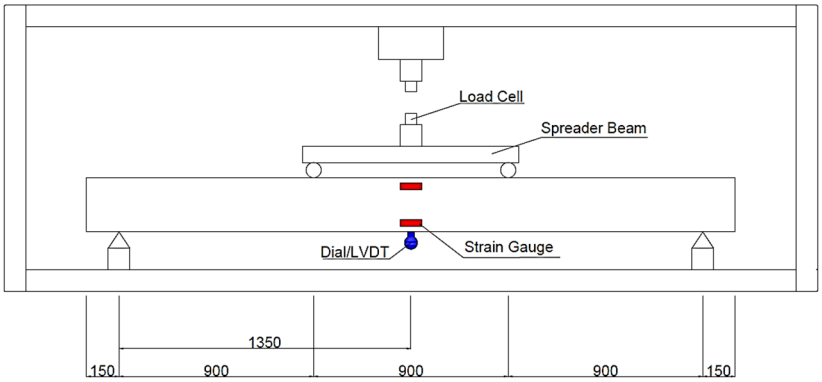


Figure 5. Testing scheme for fourth-point loading under semi-cyclic conditions.

2.3.4. Digital Image Correlation (DIC)

Digital Image Correlation (DIC) is a measurement technique used for evaluating displacement, contours, deformation, vibration, and strain. The DIC method utilized in this study represents a further advancement from previous research [21,38–41]. These studies analyzed the motion of speckles within the captured digital images of RC beam specimens' surface under a four-point load flexural test.

One side of the front surface of the RC concrete sample was painted using white paint and randomly sprayed with black acrylic paint dots using a paint gun (Figure 6). This step was carried out to prepare for DIC testing, where the analysis requires images with contrasting random dots. The created speckle pattern was examined using the GOM Correlate application to measure the pattern quality. The beam's speckle pattern is considered good if it has an average pattern quality value of around 6.0. If the value is still below 6.0, more black dots should be added to make it denser. The measurement accuracy

depends on the quality of the images taken during the experiment and should be free from geometric disturbances. The setting of fourth-point loading test and DIC analysis is presented in Figure 7.



Figure 6. Process of speckle pattern creation in RC concrete sample.



Figure 7. Setting of fourth-point loading test and DIC analysis in the laboratory.

2.4. Numerical Method: Finite Element Analysis

Utilizing the multi-fiber approach for structural modeling proves to be an efficient method for analyzing beam behavior, particularly during non-linear phases. This approach stands out from the classical finite element analysis, which often involves time-consuming calculations. The preference for the multi-fiber modeling approach in non-linear analysis stems from its effectiveness and computational efficiency.

In multi-fiber beam elements, a three-dimensional structural component (Figure 8a) is simplified into two finite element structures. A multi-fiber element consists of a two-dimensional fiber element and a one-dimensional beam element (Figure 8b).

In the multi-fiber modeling technique, beams are analyzed based on either the Euler–Bernoulli or Timoshenko beam theories. These theories provide a framework for understanding how a beam's cross-section experiences strain while undergoing deformation. According to the Euler–Bernoulli theory, the cross-section remains flat and perpendicular to the neutral axis of the beam during deformation. Conversely, the Timoshenko theory allows for the cross-section to remain flat but not necessarily perpendicular to the beam's neutral axis. It is worth noting that the Euler–Bernoulli theory may not be the most suitable choice for analyzing interactions involving axial, shear, and flexural aspects [43]. The flexibility and adaptability of the multi-fiber approach make it a valuable tool for gaining insights into complex structural behaviors.

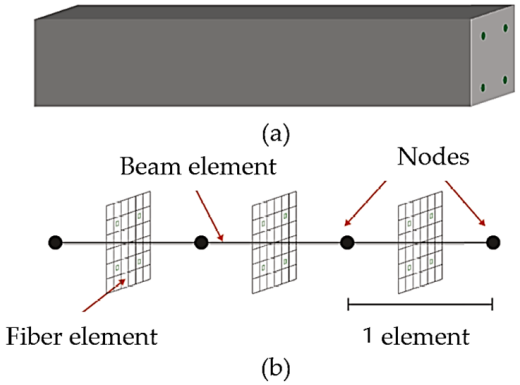


Figure 8. Multi-fiber beam element [42]: (**a**) a 3D beam structural component and (**b**) 2D fiber element and a 1D beam element.

The application of this modeling approach within CAST3M involves the use of an internal language called GIBIANE. Within this framework, users have the capability to generate objects using a variety of operators. The multi-fiber model is specifically tailored to accommodate the defined geometry and material properties within the code. This code incorporates commands designed to convert the beam into representative fibers, thereby facilitating a meticulous and precise modeling procedure. The GIBIANE language in CAST3M provides a versatile platform for users to define and manipulate objects, enhancing the flexibility and adaptability of the modeling process.

Concrete exhibits characteristics that fall into the category of anisotropic materials, making it a complex material. The properties of concrete, encompassing both linear and non-linear phases, are influenced by both material and geometric factors. When concrete is subjected to non-linear phases, permanent deformation occurs, leading to displacements, cracks, and ultimately failure if it reaches its ultimate limit. One of the damage models that describes the non-linear behavior of concrete is the Mazars' damage model.

The Mazars' damage model is a simple and robust isotropic 3D damage modeling [44,45]. This model employs damage mechanics to describe the stiffness degradation of the material due to the emergence of microscopic cracks in concrete. The constitutive relationship of the Mazars' damage model is suitable for standard concrete with compressive strength ranging from 30 to 40 MPa. The purpose of this relationship is to obtain the material's response under load, leading to deformation or elongation (uniaxial tensile stress, uniaxial compressive stress, and flexural stress in structural members). This model provides a mathematically consistent prediction of structural responses until the onset of failure due to strain localization [46].

3. Results and Discussion of Experimental Study

3.1. Compressive and Tensile Strength

The average compressive strengths of the companion cylinders for RC Beams 1, 2, and 3 are recorded at 43.36 MPa, 41.15 MPa, and 45.49 MPa, respectively (Figure 9). The average compressive strength value of the companion cylinders from the three beams is 43.3 MPa. This magnitude closely aligns with the compressive strength data obtained in previous research [21], differing by only 4.7%. The average tensile strength value of the companion cylinders from the three RC beams is 2.4 MPa. The average compressive and tensile strength values of the companion cylinders from the three RC beams will be used as one of the input parameters in creating the numerical model of the RC beam in CAST3M.

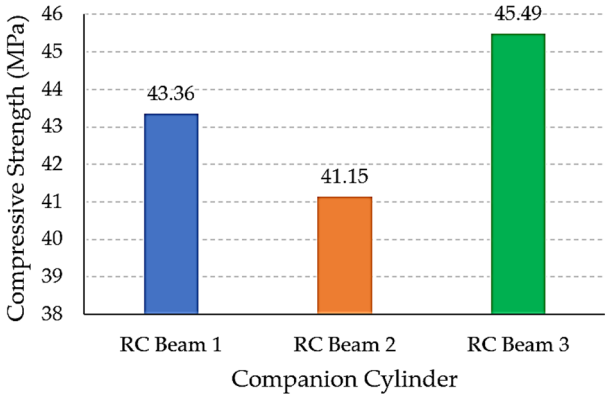


Figure 9. Average compressive strength of companion cylinder for each RC beam.

3.2. Homogeneity of RC Beam

In Figure 10, the UPV values for each RC beam are presented alongside the UPV test results and compressive strength of the companion cylinders for each beam. The UPV and compressive strength values of the companion cylinders indicate that RC Beam 3 (green) has the highest UPV and compressive strength values, followed by RC Beam 1 (blue), and then RC Beam 2 (orange).

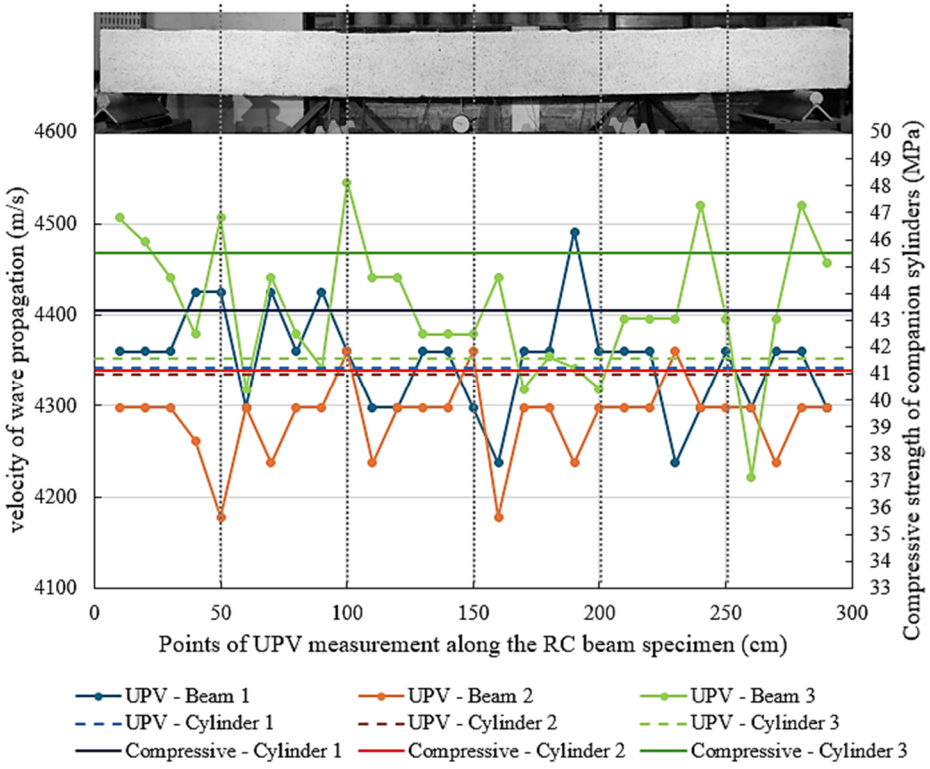


Figure 10. Homogeneity evaluation along the beam specimen.

UPV testing was conducted on the beam specimens to assess their homogeneity. The results showed variations in wave propagation velocity across the span of each beam. These differences could be attributed to variances in aggregate distribution or compaction processes during sample casting. However, the magnitude of UPV results along the beams were not significantly different. The coefficients of variation in UPV results along the spans of RC Beams 1, 2, and 3 were 1.3%, 1.0%, and 1.6%, respectively. Therefore, it can be concluded that the beam specimens exhibit relatively consistent uniformity. Following the assessment of sample homogeneity, the beams will undergo testing using the four-point loading method under semi-cyclic loading condition.

3.3. Load–Displacement of RC Beam

The load–displacement relationship obtained from LVDT and DIC method will be compared. This comparison is made to understand the differences between the two methods during each loading cycle for RC Beam 1, RC Beam 2, and RC Beam 3.

3.3.1. Load and Displacement for RC Beam 1

The comparison of load–displacement curves between LVDT and DIC measurements for RC Beam 1 across loading cycles 1, 2, 3, and 4 is shown in Figure 11.

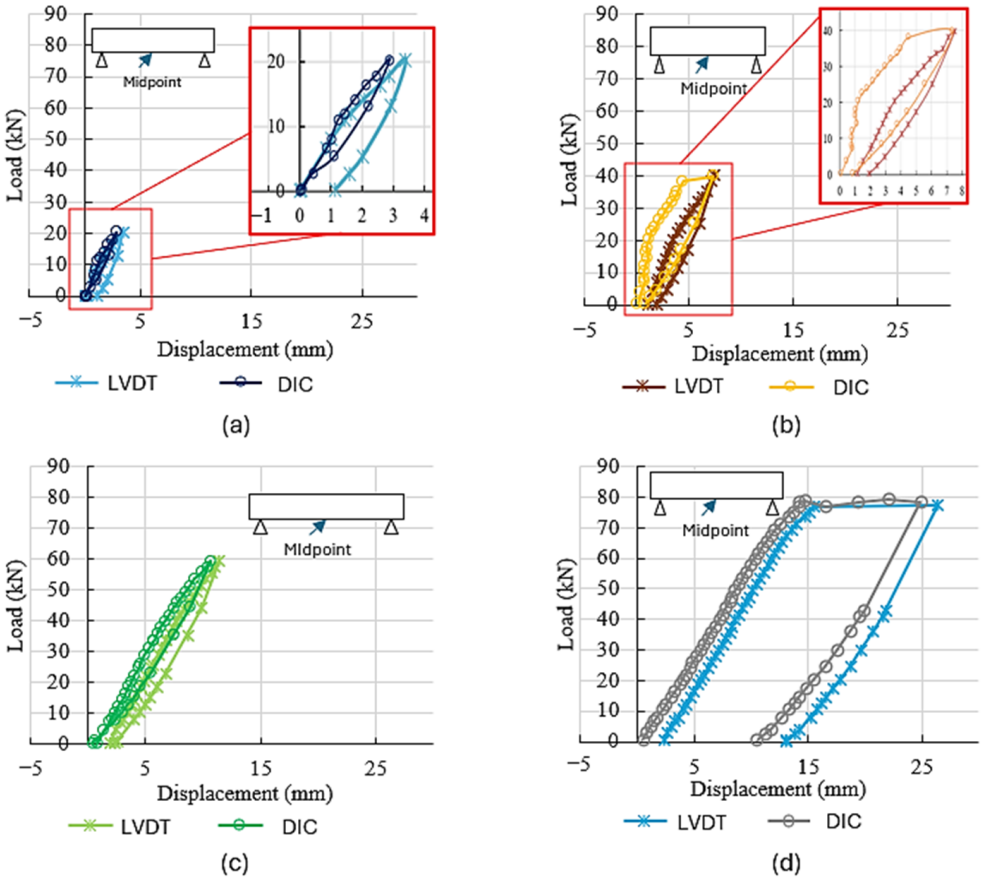


Figure 11. Load–displacement curves obtained from LVDT and DIC measurements on RC Beam 1: (**a**) Cycle 1, (**b**) Cycle 2, (**c**) Cycle 3, and (**d**) Cycle 4.

In the first cycle (Figure 11a), it is observed that the DIC results show a displacement 0.51 mm smaller than the LVDT readings at maximum load and 1.07 mm smaller upon load release. In the second cycle (Figure 11b), the DIC results indicate a displacement 0.18 mm smaller than the LVDT readings at maximum load and 1.07 mm smaller upon load release. In the third cycle (Figure 11c), the DIC results reveal a displacement 0.86 mm smaller than the LVDT readings at maximum load and 1.51 mm smaller upon load release. This consistent difference between LVDT and DIC tests on the beam suggests a recurring pattern. In the fourth cycle (Figure 11d), the maximum displacement derived from DIC analysis is also smaller than the LVDT results by 1.35 mm. Upon release of all loads, the DIC results show a displacement 2.53 mm smaller than the LVDT results. The summary of displacement values between LVDT and DIC methods for RC Beam 1 can be seen in Figure 12.

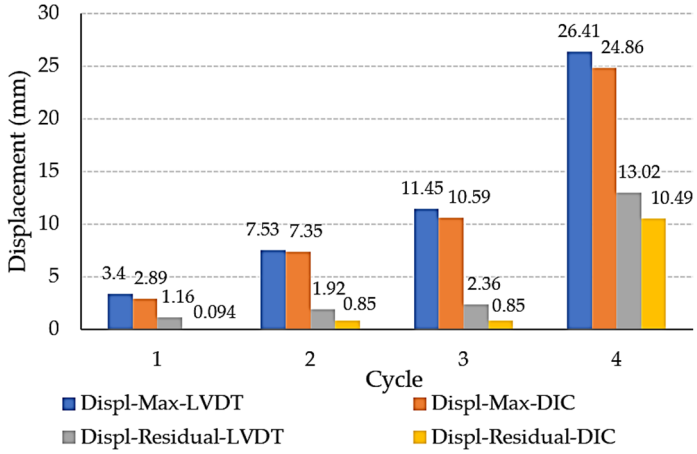


Figure 12. Displacement from LVDT and DIC on RC Beam 1.

3.3.2. Load and Displacement for RC Beam 2

The comparison of load–displacement curves between LVDT and DIC measurements for RC Beam 2 across loading cycles 1, 2, 3, and 4 is shown in Figure 13.

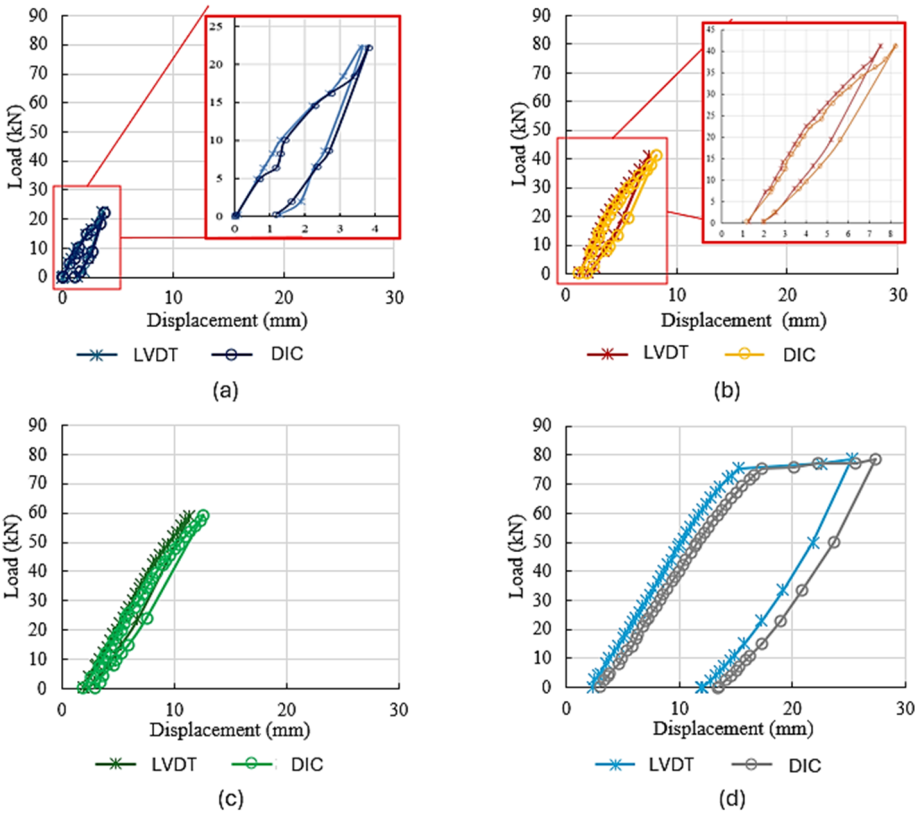


Figure 13. Load–displacement curves obtained from LVDT and DIC measurements on RC Beam 2: (**a**) Cycle 1, (**b**) Cycle 2, (**c**) Cycle 3, and (**d**) Cycle 4.

In the first cycle (Figure 13a), the DIC results exhibit a displacement deviation of 0.17 mm larger than the LVDT readings at maximum load, and 0.10 mm smaller than the LVDT readings upon load release. In the second cycle (Figure 13b), the DIC results indicate a displacement deviation of 0.72 mm larger than the LVDT readings at maximum load, and 0.003 mm smaller than the LVDT readings upon load release. In the third cycle (Figure 13c), the DIC results show a displacement difference of 1.25 mm larger than the LVDT readings at maximum load, and 0.66 mm larger upon load release. In the fourth cycle (Figure 13d), the

maximum displacement derived from DIC analysis exceeds the LVDT results by 2.12 mm. When all loads are released, the DIC results show a displacement 1.43 mm larger than the LVDT results. The summary of displacement values between LVDT and DIC methods for RC Beam 2 can be seen in Figure 14.

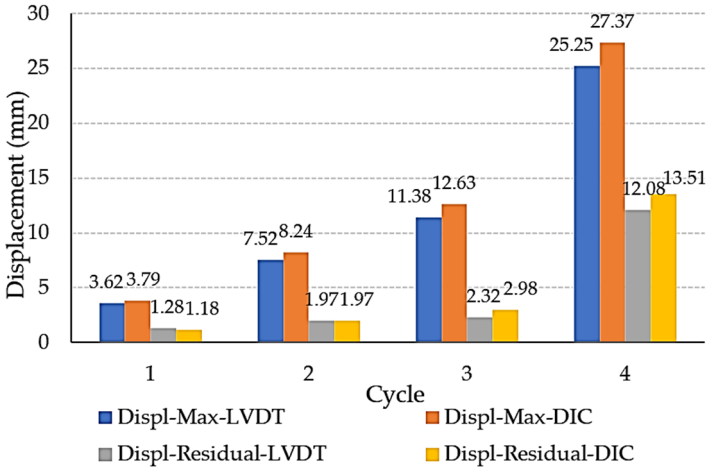


Figure 14. Displacement from LVDT and DIC on RC Beam 2.

3.3.3. Load and Displacement for RC Beam 3

The comparison of load–displacement curves between LVDT and DIC measurements for RC Beam 3 across loading cycles 1, 2, 3, and 4 is shown in Figure 15.

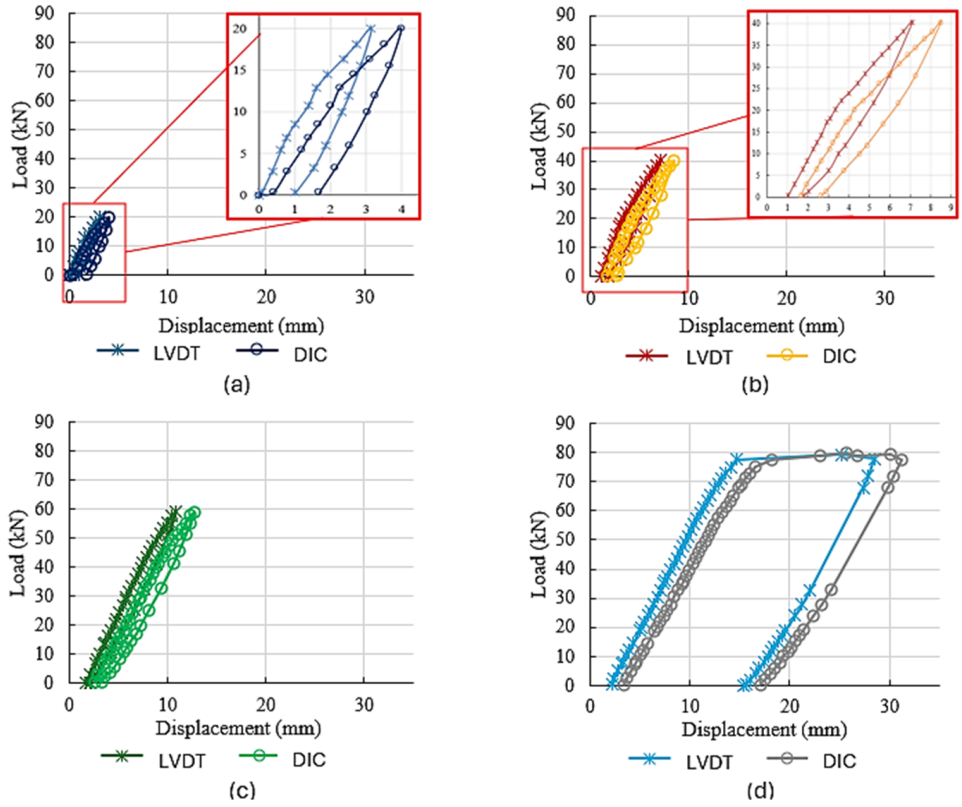


Figure 15. Load–displacement curves obtained from LVDT and DIC measurements on RC Beam 3: (**a**) Cycle 1, (**b**) Cycle 2, (**c**) Cycle 3, and (**d**) Cycle 4.

In the first cycle (Figure 15a), the DIC results show a displacement deviation of 0.83 mm larger than the LVDT readings at maximum load and 0.66 mm larger upon load

release. In the second cycle (Figure 15b), the DIC results demonstrate a displacement deviation of 1.38 mm larger than the LVDT readings at maximum load and 0.85 mm larger upon load release. In the third cycle (Figure 15c), the DIC results indicate a displacement deviation of 1.93 mm larger than the LVDT readings at maximum load and 1.18 mm larger upon load release. Finally, in the fourth cycle (Figure 15d), the DIC results exhibit a displacement deviation of 2.46 mm larger than the LVDT readings at maximum load during the elastic phase. Moreover, the maximum displacement derived from DIC analysis surpasses the LVDT results by 2.73 mm. When all the loads are released, the DIC results show a displacement 1.64 mm larger than the LVDT results. The summary of displacement values between LVDT and DIC methods for RC Beam 3 can be seen in Figure 16.

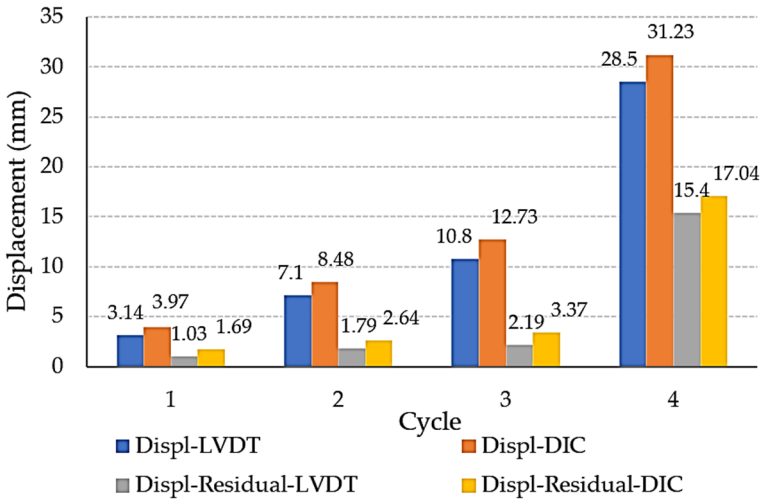


Figure 16. Displacement from LVDT and DIC on RC Beam 3.

The summary of load vs. displacement between LVDT readings and DIC method for the three RC beam samples can be seen in Table 4. The displacement values generated by the DIC method seem to exhibit the best performance in Cycle 4. It can be seen from the difference values produced, which are less than 10% compared to the LVDT readings for all three RC beams. Compared to the displacement results, the magnitude of residual displacement generated by the DIC method appears to exhibit lower performance in Cycle 4, with differences ranging between 10–20%. The DIC method provides smaller differences compared to LVDT readings for maximum displacement results in comparison to residual displacement for all loading cycles in all RC beam specimens. The differences in the results between LVDT and DIC methods highlight the impact of image distortion during the beam loading process. Nevertheless, both methods exhibit similar behavior in their outcomes. Despite this difference, the alignment in behavior between the two methods underscores their complementary nature in structural assessment, providing valuable insights into material response under loading conditions.

Table 4. Summary of load vs. displacement for each RC beam specimens.

Sample RC Beam	Cycle	Load (kN)	Displacement (mm)					
			Displacement			Residual Displacement		
			LVDT	DIC	Difference	LVDT	DIC	Difference
1	1	20.40	3.4	2.89	0.51 (15%)	1.16	0.094	1.07(91.9%)
	2	39.83	7.53	7.35	0.18 (2.4%)	1.92	0.85	1.07 (55.7%)
	3	59.45	11.45	10.59	0.86 (7.5%)	2.36	0.85	1.51 (64%)
	4	78.87	26.41	24.86	1.55 (5.9%)	13.02	10.49	2.53 (19.4%)

Table 4. *Cont.*

Sample RC Beam	Cycle	Load (kN)	Displacement (mm)					
			Displacement			Residual Displacement		
			LVDT	DIC	Difference	LVDT	DIC	Difference
2	1	22.17	3.62	3.79	−0.17 (4.7%)	1.28	1.18	0.10 (7.8%)
	2	41.2	7.52	8.24	−0.72 (9.6%)	1.97	1.97	0.003 (0.2%)
	3	59.15	11.38	12.63	−1.25 (11%)	2.32	2.98	−0.66 (28.4%)
	4	78.77	25.25	27.37	−2.12 (8.4%)	12.08	13.51	−1.43 (11.8%)
3	1	20.01	3.14	3.97	−0.83 (26.4%)	1.03	1.69	−0.66 (64.1%)
	2	40.22	7.1	8.48	−1.38 (19.4%)	1.79	2.64	−0.85 (47.5%)
	3	59.15	10.8	12.73	−1.93 (17.9%)	2.19	3.37	−1.18 (53.9%)
	4	79.66	28.5	31.23	−2.73 (9.6%)	15.4	17.04	−1.64 (10.6%)

3.3.4. Load and Displacement Relationship of the RC Beams

Analysis of maximum and residual displacement measurements using both the LVDT readings and DIC method gives differences in results up to 10% and 20%, respectively. Following loading to the plastic phase, deflections in all three RC beam samples tend to revert to their original shape. This indicates that the beams retain elastic properties from the steel reinforcement. Considering theoretical calculations of the reinforced concrete beam capacity, it is evident that the tensile and compressive reinforcement in the beams have not yielded, while the concrete has reached its capacity. Consequently, this leads to relatively minor residual deflection in the beams after loading.

From the results of the load-displacement relationship, there is a change in stiffness or slope in the load vs displacement graph for RC beams as shown in the red circle in Figure 17. The tensile stress values occurring at the bottom fiber of the concrete when the load reaches the point of slope change in the graph can be seen in Table 5. Based on the stress calculation results, it is evident that Beams 1 and 3 have reached their tensile strength capacities, while Beam 2 is approaching its tensile strength capacity. These results can explain the stiffness changes due to the loss of tensile stiffness from the concrete as it has reached its tensile capacity. Stiffness changes indicate the initiation of crack localization in the concrete [38].

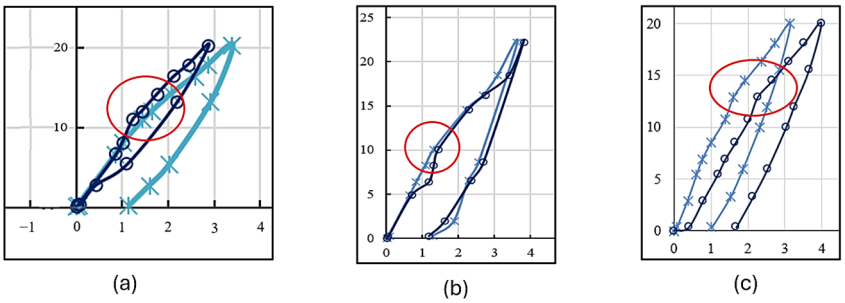


Figure 17. Stiffness changes in: (**a**) RC Beam 1, (**b**) RC Beam 2, and (**c**) RC Beam 3.

Table 5. Tensile stress at the bottom fiber of the beam during stiffness changes.

RC Beam	2P (kN)	M (kNm)	σ (MPa)	Tensile Strength (MPa)
1	10.99	4.94	3.16	1.93
2	10.10	4.55	2.91	3.08
3	12.85	5.78	3.70	2.42

3.3.5. Load–Displacement Curves with Other Similar Studies

In this section, a comparison will be presented of the load–displacement curve results obtained from the DIC method and the same type of testing, namely the fourth-point loading test under semi-cyclic loading conditions. The study examines RC beams with identical dimensions and reinforcement details but different concrete types. Handika et al. [47] assessed the displacement of normal RC beams using the DIC method, while another study investigated the impact of incorporating oil palm shell waste (OPS) in concrete mixtures on mechanical properties using the same DIC method [48].

The comparison of load–displacement curves obtained from the DIC method for normal RC beams, OPS RC beams, and FNS RC beams is shown in Figure 18. Observations during cycles 1–4 of loading reveal that the slope of the FNS RC Beam curve is notably higher compared to those of the Normal RC Beam and OPS RC Beam, indicating greater stiffness and delayed crack development. Upon unloading in Cycle 4, the slopes of the Normal RC Beam and FNS RC Beam curves are nearly identical. In contrast, the OPS RC Beam curve exhibits the shallowest slope among the three, indicating the lowest stiffness relative to the Normal RC Beam and FNS RC Beam.

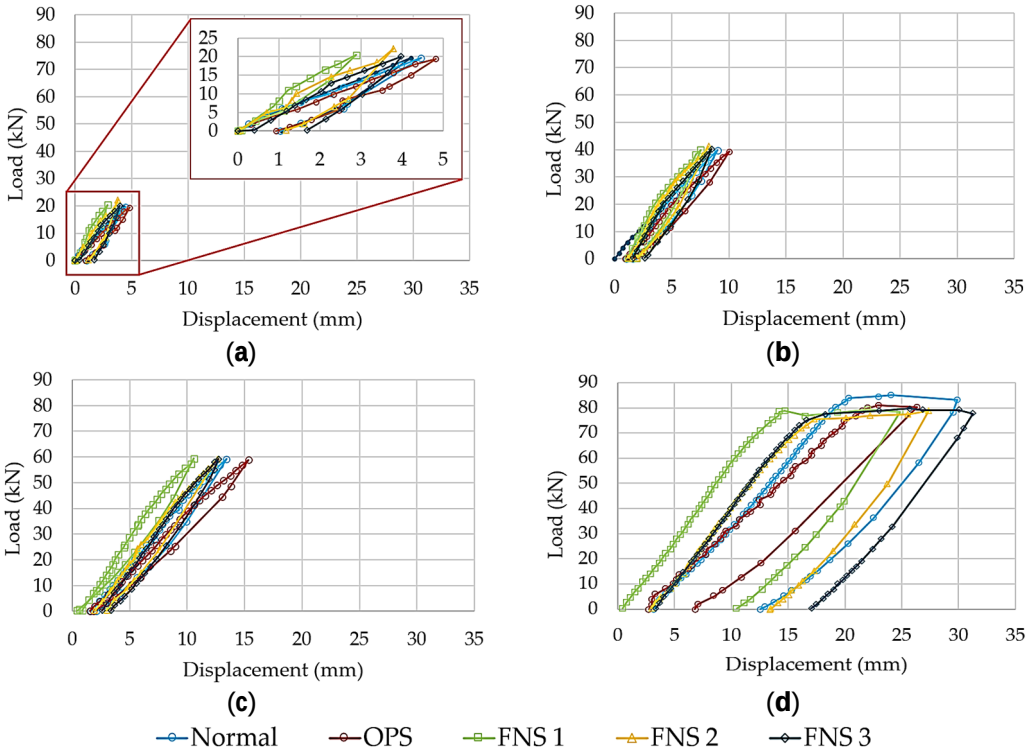


Figure 18. Comparison of load–displacement curves between Normal RC Beam (Normal) [47], OPS RC Beam (OPS) [48], and FNS RC Beam (FNS 1, FNS 2, FNS 3) for: (**a**) Cycle 1, (**b**) Cycle 2, (**c**) Cycle 3, and (**d**) Cycle 4.

The magnitudes of maximum displacement and residual displacement for Cycles 1 to 4 for the Normal RC Beam, OPS RC Beam, and average FNS RC Beam can be seen in Figure 19. The maximum displacement value of the FNS RC Beam is smaller than that of the Normal RC Beam for all cycles. In Cycle 4, the maximum displacement of the FNS RC Beam is 7% less than that of the Normal RC Beam. Conversely, the FNS RC Beam exhibits higher residual displacement compared to the Normal RC Beam and the OPS RC Beam. In Cycle 4, the residual displacement of the FNS RC Beam is 8.7% greater than that of the Normal RC Beam.

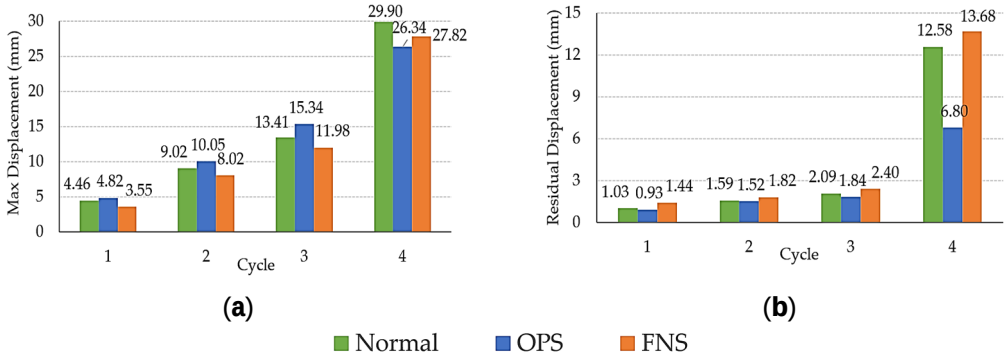


Figure 19. Displacement results for Normal RC Beam (Normal) [47], OPS RC Beam (OPS) [48], and average FNS RC Beam (FNS): (**a**) maximum displacement, and (**b**) residual displacement.

The difference in results between the FNS RC Beam and the Normal RC Beam, showing a difference of less than 10% in Cycle 4, indicates that using 50% FNS as a substitute for fine aggregate can yield behavior nearly identical to normal concrete in the final cycles of semi-cyclic loading. The utilization of FNS could be considered as a response to environmental issues and may be effectively utilized in reinforced concrete beams.

3.4. Strain Analysis

Strain gauges were positioned along both the top and bottom fibers of the beam to measure strain. Positioned at the mid-span, these gauges captured both tensile and compressive strains caused by the load. These gauges were then interfaced with a National Instruments (NI) computing device, which was connected to a computer running LabVIEW National Instruments software Version 2022 Q3. The readings from these strain gauges were subsequently synchronized with the applied load on the beam to quantify the strain.

The relationship between the load and strain for the three RC beams in each loading cycle can be observed in Figure 20. Table 6 presents the magnitude of maximum strain measurements and strain after the unloading phase for the three RC beams in each cycle.

Table 6. Strain measurement for each RC Beam specimens.

Sample RC Beam	Cycle	Strain			
		Top Fiber		Bottom Fiber	
		Maximum	After Unloading	Maximum	After Unloading
1	1	−0.0004	0.00008	0.0008	0.00023
	2	−0.0007	−0.00010	0.0015	0.00005
	3	−0.0010	−0.00012	0.0024	−0.00011
	4	−0.0020	−0.00083	0.0035	0.00036
2	1	0.00001	0.00024	0.0007	0.00033
	2	−0.00018	0.00027	0.0016	0.00039
	3	−0.00031	0.00046	0.0025	0.00058
	4	−0.00044	0.00068	0.0035	0.00097
3	1	−0.0003	0.00025	0.0005	0.00039
	2	−0.0005	−0.00006	0.0008	0.00053
	3	−0.0008	0.00008	0.0013	0.00066
	4	−0.0017	−0.00073	0.0019	0.00068

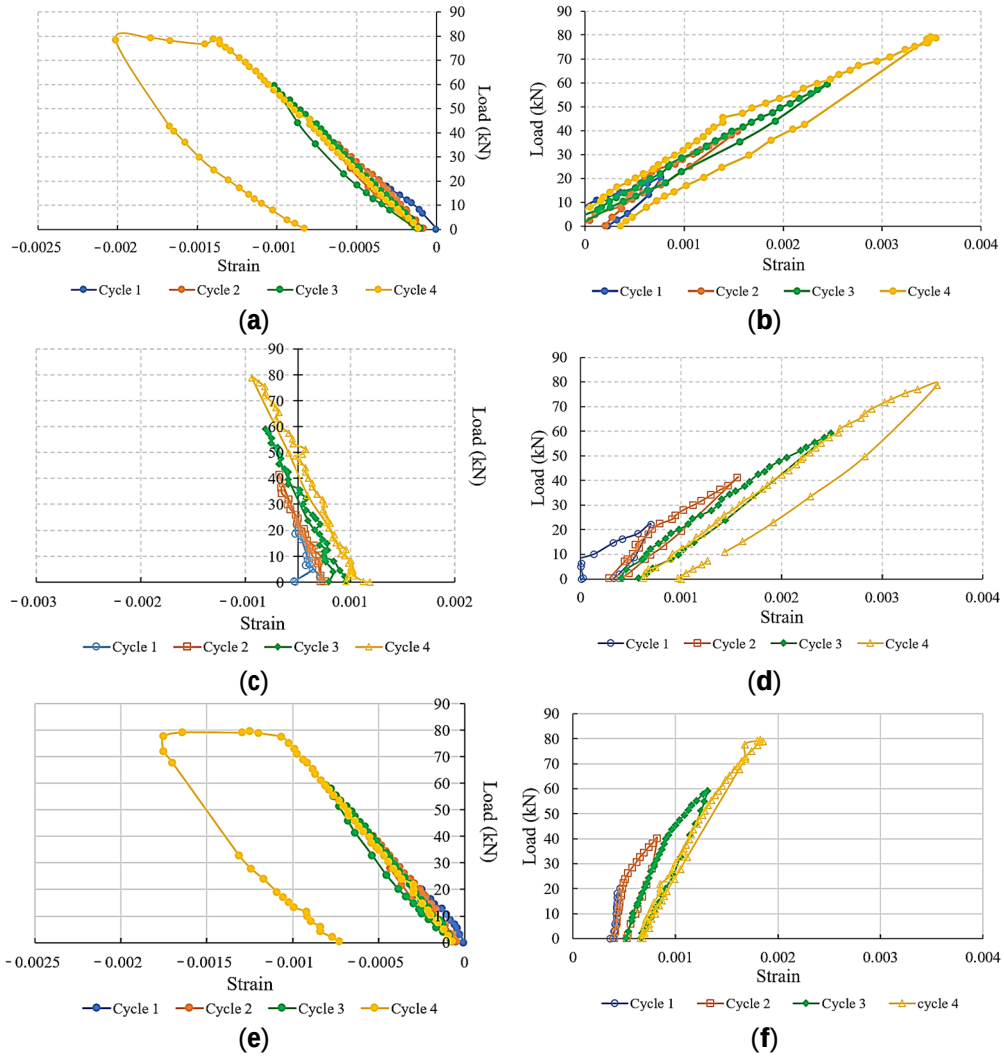


Figure 20. Load vs. strain curve: (**a**) RC Beam 1—top fiber, (**b**) RC Beam 1—bottom fiber, (**c**) RC Beam 2—top fiber, (**d**) RC Beam 2—bottom fiber, (**e**) RC Beam 3—top fiber, and (**f**) RC Beam 3—bottom fiber.

The strain gauge readings on the upper part of RC Beam 1 and RC Beam 3 appear to be consistent with the theory, where the upper fiber strain of the beam has negative values or compressive strain. The load vs. strain graph illustrates similar behavior between RC Beam 1 and RC Beam 3, but differing behavior is shown in RC Beam 2. The accuracy of the measurements may be affected by a range of errors originating from bonding quality, wire effects, and temperature variations [49].

In the fourth cycle, the strain gauge readings for the bottom fibers of RC Beams 1 and 2 (Figure 20b,d) show that they have surpassed the critical strain of concrete by 0.003, as presented in Table 6 where it equals 0.0035. This could indicate the presence of microcracks [50] in the middle span of the beam under a load of 80 kN. The strain gauge readings on the bottom part of all RC beams appear to align with theory, where the strain on the bottom fiber of the beam shows positive values, indicating tensile strain.

3.5. Surface Deformation

The analysis of beam deformation utilizes the Digital Image Correlation (DIC) method, facilitated by the GOM Correlate application. This method meticulously examines surface deformations of the beam, utilizing data extracted from the examination of major strain (ε_{11}) within the GOM Correlate application. This detailed examination allows for correlating surface deformations with the loads applied to the beam, while ensuring the exclusion of the beam's self-weight influence. By isolating external loads from internal structural effects,

this approach enables a thorough investigation into the origin of cracks and their precise locations across the beam's surface.

When dividing the surface area of the beam, four key points are identified. Points A and D represent the supports of the beam, providing stable reference points for its structural integrity. In contrast, points B and C denote the exact locations where loading from the spreader beam is applied onto the beam under examination. This segmentation of the surface area provides a detailed perspective, distinguishing regions subjected to different force interactions.

The area extending from points A to C, and C to D, becomes a focal point where both bending moment and shear forces converge, exerting varying degrees of influence on the structural integrity of the beam. This interplay of dual forces creates intricate stress distributions within the beam, requiring a nuanced approach to comprehend deformation patterns and crack formations. Conversely, the segment between points B and C is predominantly subjected to bending moment forces, as determined through meticulous statics analysis.

3.5.1. Surface Deformation RC Beam 1

In Figure 21a, the deformation progression of RC Beam 1 throughout its first cycle was presented. Notably, a pristine surface without any cracks remains intact until a significant load is applied, signaling the beginning of structural transformation. At an applied load of 1120 kgf or 11 kN, the beam shows resilience. However, as the load increases to 1680 kgf (16.5 kN), the appearance of vertical cracks near the B–C area marks a significant transition. These cracks continue to propagate, reaching the C–D region as the load intensifies to 2080 kgf (20.4 kN).

In Figure 21b, Beam 1's deformation progression during its second cycle provides was shown. The appearance of subtle yet discernible vertical cracks in the B–C region at a load of 1050 kgf (10.3 kN), signifying the beginning of structural transformation, which gradually becomes more prominent as the load increases. At 2080 kgf (20.4 kN), these cracks take on a more pronounced light blue, persisting and spreading until reaching the peak load of the second cycle at 4060 kgf (39.8 kN). The largest vertical cracks appear in the B–C area, extending their reach to encompass the A–B and C–D regions. Although the cracks due to friction in the A–B and C–D areas are not fully visible yet, the formation of vertical cracks continues to occur.

In Figure 21a,c, thorough examination reveals the intricate progression of Beam 1's deformation throughout its third cycle. The appearance of vertical cracks in the B–C area at a load of 2040 kgf (20 kN) was observed. These cracks, extending to include the A–B and C–D areas, progressively enlarge as the load gradually increases, reaching a peak at 6060 kgf (59.4 kN). Of particular interest is the evolving behavior of cracks within the A–B and C–D regions, which gradually transition towards shear-induced patterns, as evidenced by the emergence of inclined cracks.

Figure 21d illustrates the evolution of Beam 1's deformation during the fourth cycle. Light blue vertical cracks appear within the B–C region, becoming prominent until the load reaches 6100 kgf (59.8 kN). At a load of 8040 kgf (78.9 kN), the beam reaches the peak of its elastic phase, characterized by visible cracks across the A–B, B–C, and C–D regions. The evident inclined cracks, attributed to shear-induced deformation, were observed within the A–B and C–D areas. After passing the elastic phase, the beam continues to endure loading until entering the plastic regime. At a load of 8080 kgf (79.3 kN), three prominent red vertical cracks emerge within the B–C area during the plastic phase. Consequently, these cracks experience sustained enlargement, while others experience relatively minor expansion, emphasizing localized stress concentration.

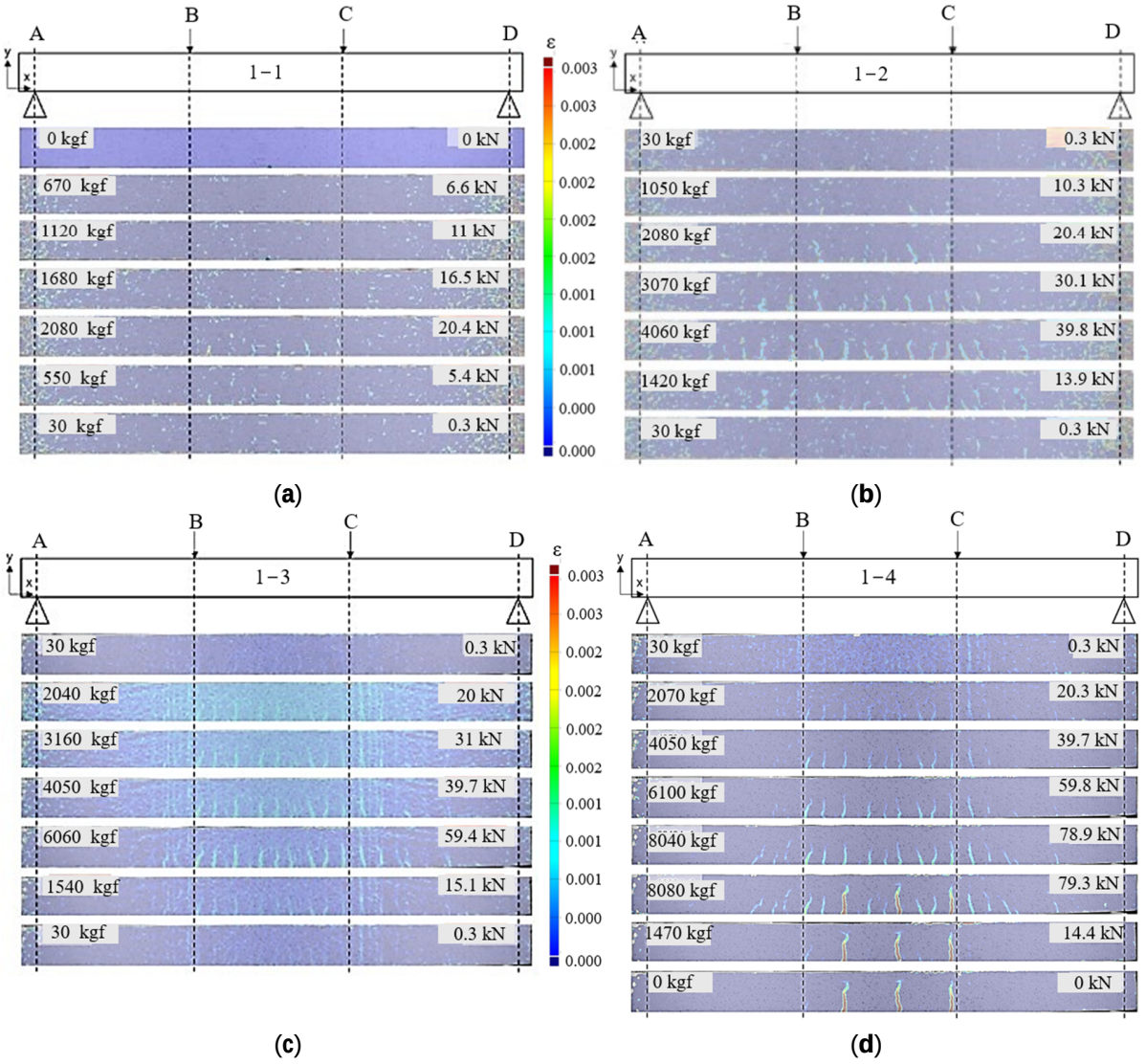


Figure 21. Evolution of surface deformation in RC Beam 1 covering the A–D region: (**a**) Cycle 1, (**b**) Cycle 2, (**c**) Cycle 3, (**d**) Cycle 4.

3.5.2. Surface Deformation RC Beam 2

In Figure 22a, the comprehensive evolution of Beam 2's deformation during the first cycle will be presented. A significant noise was observed on the left side of point A and the right side of point D. This phenomenon arises from the camera's focal limitations in capturing the beam's end sections sharply, which can be attributed to differences in distance between the camera and the beam's center versus its ends. Until a load of 1490 kgf (14.6 kN) is applied, no significant cracks are evident on the beam's surface. However, at a load of 2260 kgf (22.2 kN), faint light blue vertical cracks begin to emerge in the B–C area, attributed to pure moment stresses. Following gradual load release, the visible cracks close again.

Figure 22b presents the deformation evolution observed in RC Beam 2 during its second cycle. Initially, subtle vertical cracks emerge within the B–C area at a load of 1050 kgf (10.3 kN), signaling the beginning of the structural response to applied loads. These cracks gradually intensify, transitioning from light blue to red hues, as the load increases to 2070 kgf (20.3 kN), highlighting the progressive nature of deformation under escalating loads. When reaching 3060 kgf (30 kN), the vertical cracks in the B–C area become more pronounced and extend into the A–B and C–D regions. As the load peaks at 4200 kgf (41.2 kN), the appearance of inclined cracks in the C–D area indicates shear-induced deformation.

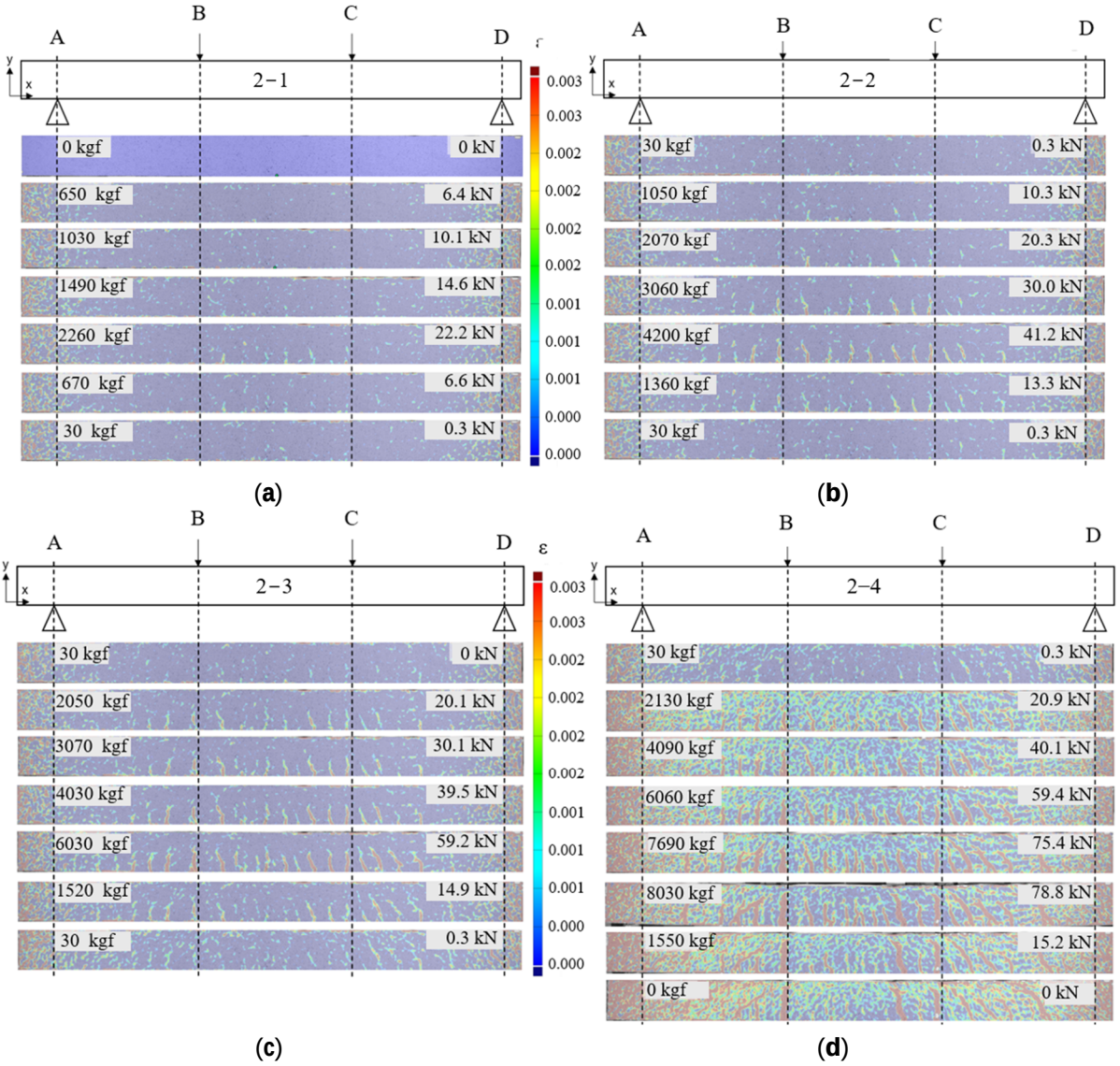


Figure 22. Evolution of surface deformation in RC Beam 2 covering the A–D region: (**a**) Cycle 1, (**b**) Cycle 2, (**c**) Cycle 3, (**d**) Cycle 4.

Figure 22c illustrates the evolving deformation results of RC Beam 2 during its third cycle. The presence of red cracks at a load of 2050 kgf (20.1 kN), spanning across the A–B, B–C, and C–D areas, indicates a significant structural response to the applied load. As the load increases to 6030 kgf (59.2 kN), these cracks progressively widen, emphasizing the critical influence of load magnitude on crack propagation. The distribution of vertical cracks attributed to bending moments within the B–C area, along with the formation of inclined cracks in the A–B and C–D regions around load points B and C, aligns with classical beam theory. This theory predicts stress concentrations and crack initiation at points of maximum bending stress [51].

Figure 22d presents the deformation evolution of RC Beam 2 during its fourth cycle. The presence of noise on the strain plane indicates potential variations in image quality captured by the camera. However, clear indications of both vertical and inclined cracks are evident across the A–B, B–C, and C–D areas, becoming prominent at a load of 2130 kgf (20.9 kN). As the load reaches 7690 kgf (75.4 kN), further crack enlargement and structural deformation were present. The progression of cracks intensifies as the beam transitions into the plastic phase at a load of 8030 kgf (78.8 kN), with two significant cracks emerging in the B–C area and one prominent crack beneath load point B.

3.5.3. Surface Deformation RC Beam 3

Figure 23a illustrates the deformation evolution of RC Beam 3 during its first cycle. The areas adjacent to the left point A and right point D exhibit significant noise, attributed to the camera's inability to sharply capture the beam's endpoints due to differing distances from the camera to the beam's center and endpoints. Until a load of 1660 kgf (16.3 kN) is applied, no significant cracks are observed on the beam's surface. However, at a load of 2040 kgf (20 kN), subtle light blue to yellowish vertical cracks begin to emerge in the B–C area, indicative of crack propagation due to pure bending moment [38].

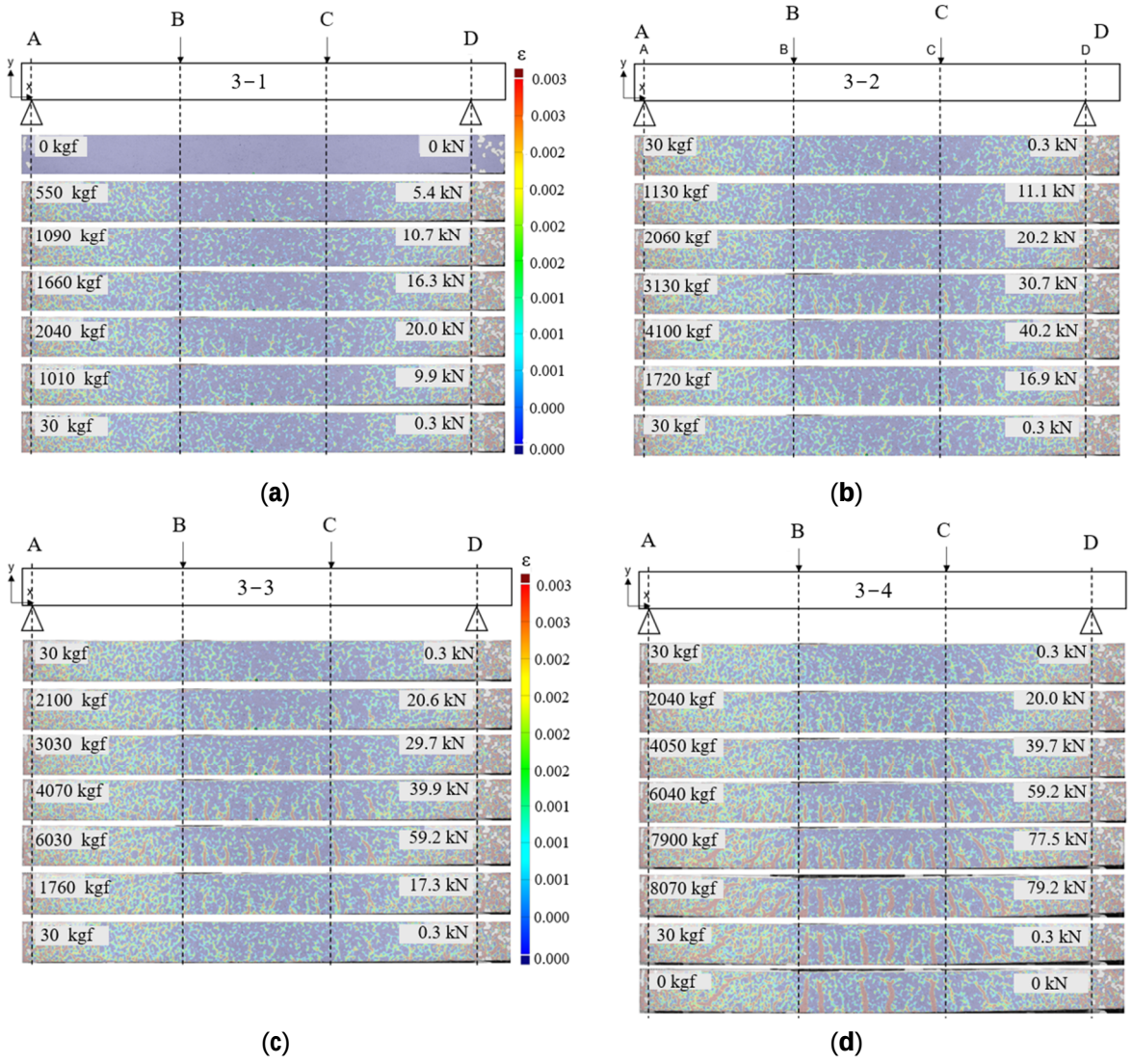


Figure 23. Evolution of surface deformation in RC Beam 3 covering the A-D region: (**a**) Cycle 1, (**b**) Cycle 2, (**c**) Cycle 3, (**d**) Cycle 4.

Figure 23b illustrates the deformation evolution of RC Beam 3 during its second cycle, offering insights into its structural response under varying loading conditions. It is observed that fine vertical cracks occur in the B–C area at a load of 2060 kgf (20.2 kN). These cracks become more pronounced (light blue and red) as the load increases, spreading to the A–B and C–D areas at a load of 3130 kgf (30.7 kN). The cracks continue to enlarge until the load reaches 4100 kgf (40.2 kN).

Figure 23c illustrates the deformation evolution of RC Beam 3 during its third cycle. It is evident that cracks (red) continue to propagate across the A–B, B–C, and C–D areas as the load reaches 2100 kgf (20.6 kN). These cracks progressively enlarge with increasing load,

reaching their maximum extent at 6030 kgf (59.2 kN). Vertical cracks induced by moments are predominantly distributed in the B–C area, while diagonal cracks in the A–B and C–D areas form around load points B and C.

Figure 23d presents the deformation evolution of RC Beam 3 during its fourth cycle. Vertical and diagonal cracks (depicted in red) are prominently visible along the entire span of the A–B, B–C, and C–D regions at a load of 4050 kgf (39.7 kN). As the load reaches 7900 kgf (77.5 kN), RC Beam 3 reaches the peak of its elastic phase, with cracks progressively enlarging as it transitions into the plastic phase at a load of 8070 kgf (79.2 kN). Notably, five significant cracks are observed in the B–C area, discernible from the extensive, red-colored local strain areas associated with these cracks. While both the hydraulic load and the spreader beam are fully released. While smaller cracks in the A–B and C–D areas close upon load removal, the five significant cracks in the B–C area remain open.

The crack propagation along the B–C axis during Cycle 1 for all RC beams is primarily attributed to pure bending moment. As the load is gradually released, these observed cracks tend to close. At the end of the cycle, despite full release of the hydraulic load (with only the load from the spreader beam remaining), the strain does not fully return to its initial pre-loaded state. This behavior is due to residual deformation within the beam, which contributes to the formation of localized residual cracks on the beam's surface [38].

In the second cycle, the vertical cracks in the B–C area become more pronounced, extending further into both the A–B and C–D regions for all RC beams. At this load, diagonal cracks due to shear begin to appear in the A–B area. This extensive propagation of cracks highlights the significant influence of load magnitude on structural integrity, a phenomenon extensively studied in fracture mechanics. Local opening and closing of cracks are observed during the gradual application and release of load. By the end of the cycle, with the complete release of the hydraulic load and only residual load from the spreader beam remaining, the strain does not fully return to its pre-loaded state, underscoring the presence of residual stresses and deformations.

In the third cycle, the vertical cracks observed in the B–C area, resulting from bending moments, coincide with the appearance of inclined cracks in the A–B and C–D regions due to shear. As the load is gradually released, the visible cracks begin to close gradually, indicating partial structural recovery. However, similar in the previous cycle, residual strains remain apparent as indicated by the incomplete return to the pre-loaded state.

In the fourth cycle, as the load reaches a certain magnitude, the RC beams enter the peak value of their elastic phase, with cracks gradually enlarging as they transition into the plastic phase at maximum load. While both the hydraulic load and the spreader beam are fully released, resulting in a state where significant cracks remain open, in contrast to the closure observed in other smaller cracks. The progressive widening of larger cracks and narrowing of smaller ones highlights the complex behavior of the structural element under semi-cyclic loading.

The DIC method can capture crack evolution phenomena on concrete surfaces. By unraveling the intricate interplay between applied loads and resulting deformations, this analytical framework not only illuminates the evolution of beam deformation but also provides insights into potential failure modes, such as crack initiation and propagation. Through this comprehensive approach, engineers can proactively address structural vulnerabilities and devise effective mitigation strategies to maintain the beam's operational integrity and safety standards. Moreover, understanding these deformation patterns is essential for informing structural integrity assessments, directing maintenance, and repair strategies to ensure the continued safety and reliability of engineering structures.

3.6. Crack Propagation

Crack propagation analysis on the beam is performed using the DIC method. Initially, a crack is identified based on the strain fields of the beam obtained from the deformation evolution analysis. Then, two observation points are added on the left and right sides of the identified crack. The horizontal displacement (dX) values of these two points are extracted

from GOM Correlate. Subsequently, the difference in horizontal displacement between these two points is calculated, representing the width of the observed crack.

The analysis focuses on the propagation of the three largest cracks in the B–C area, which experience pure bending, and the two largest cracks in both the A–B and C–D areas, which experience shear-bending for each RC beam sample. In the following subsection, an evaluation of crack propagation due to flexural and flexural–shear behaviors will be presented.

3.6.1. Crack Propagation of RC Beam 1

Figure 24 shows the crack locations observed in RC Beam 1. An analysis will be conducted on flexural crack number 2 in the B–C region of RC Beam 1, due to pure bending. Furthermore, the diagonal flexural–shear crack number 5 in the C–D region will also be analyzed.

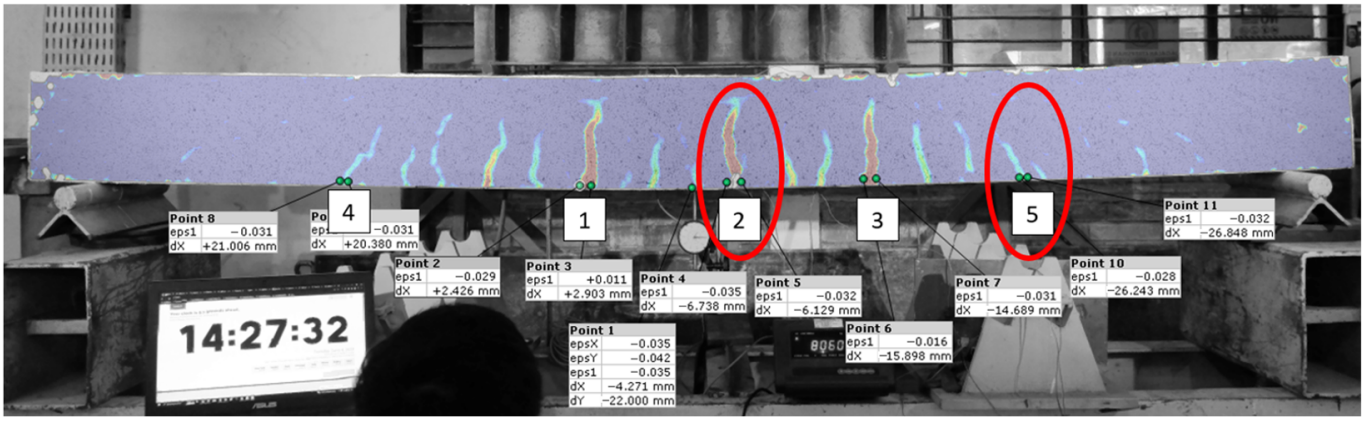


Figure 24. Crack observation points on RC Beam 1: three largest cracks in the B–C area (number 1, 2, and 3) and two largest cracks in both the A–B and C–D areas (number 4 and 5).

Figure 25a shows the propagation of flexural crack number 2 in RC Beam 1 throughout each loading cycle. Initially, the crack width reaches 0.068 mm at the maximum load of the first cycle, increasing to 0.156 mm upon load release. Subsequently, during the second cycle's maximum load, the crack width reaches 0.615 mm, increasing to 0.725 mm after unloading. Upon reaching the maximum load of the third cycle, the crack width measures 0.677 mm, increasing to 0.884 mm after load release. In the fourth cycle, the crack width peaks at 0.776 mm during the elastic phase and reaches at 0.742 mm in the plastic phase. Upon unloading, the crack width decreases to 0.305 mm.

Figure 25b presents the propagation of crack number 5 in RC Beam 1 across each loading cycle. Initially, the crack width measures 0.052 mm at the maximum load of the first cycle, increasing to 0.088 mm upon unloading. During the second cycle's peak load, the crack width expands to 0.421 mm and then to 0.484 mm after unloading. Upon reaching the maximum load of the third cycle, the crack width measures 0.565 mm, increasing further to 0.656 mm after unloading. In the fourth cycle, the crack width peaks at 0.648 mm during the elastic phase and reaches at 0.606 mm in the plastic phase. Upon unloading, the crack width increases to 0.770 mm.

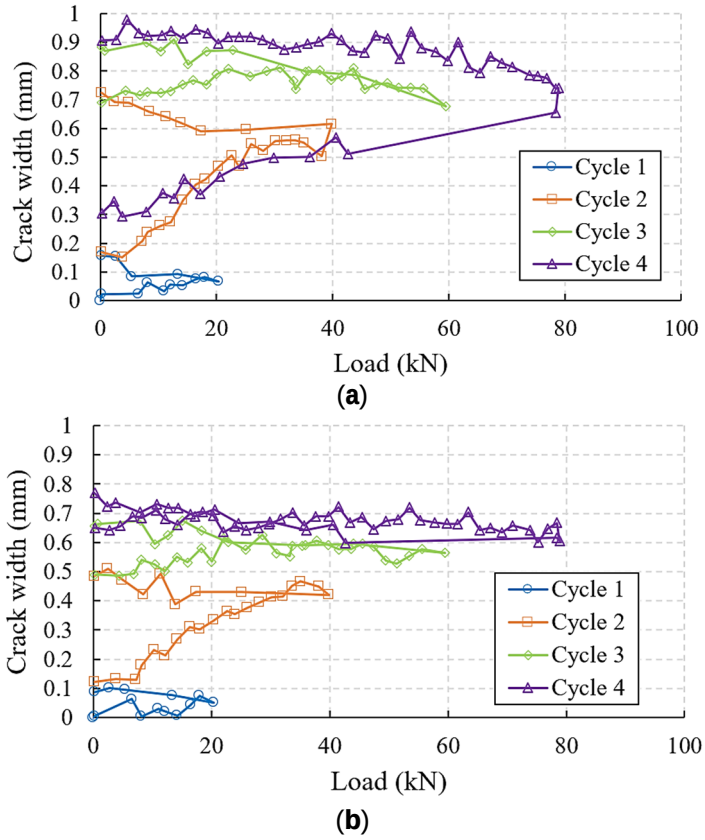


Figure 25. Crack propagation on RC Beam 1 due to: (**a**) flexural crack, and (**b**) flexural–shear crack.

3.6.2. Crack Propagation of RC Beam 2

Figure 26 shows the crack locations observed in RC Beam 2. An analysis will be conducted on flexural crack number 3 in the B–C region of RC Beam 2, due to pure bending. Furthermore, the diagonal flexural–shear crack number 4 in the C–D region will also be analyzed.

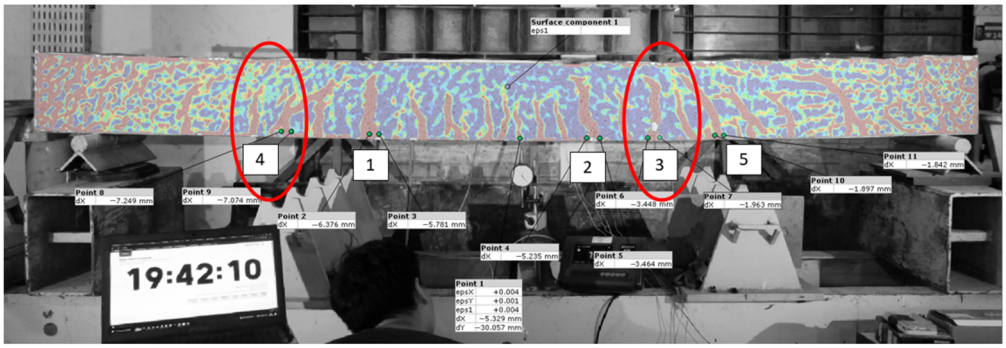


Figure 26. Crack observation points on RC Beam 2: three largest cracks in the B–C area (number 1, 2, and 3) and two largest cracks in both the A–B and C–D areas (number 4 and 5).

Figure 27a illustrates the propagation of crack number 3 in RC Beam 2 for each loading cycle. Initially, at the maximum load of the first cycle, the crack width measures 0.055 mm, increasing to 0.060 mm upon unloading. During the second cycle, the crack width initially decreases and then increases as loading progresses. At the maximum load of the second cycle, the crack width is 0.070 mm, decreasing to 0.021 mm upon unloading. Similarly, in the third cycle, the crack width follows a similar trend of initial decrease followed by increase with loading. At the maximum load of the third cycle, the crack width measures

0.124 mm, decreasing to 0.013 mm upon unloading. In the fourth cycle, the crack width continues to increase until the beam reaches the peak of the elastic phase, where it measures 0.359 mm. Subsequently, as the beam transitions into the plastic phase, the crack width significantly increases to a maximum of 1.532 mm. Upon unloading, the crack width decreases to 1.274 mm.

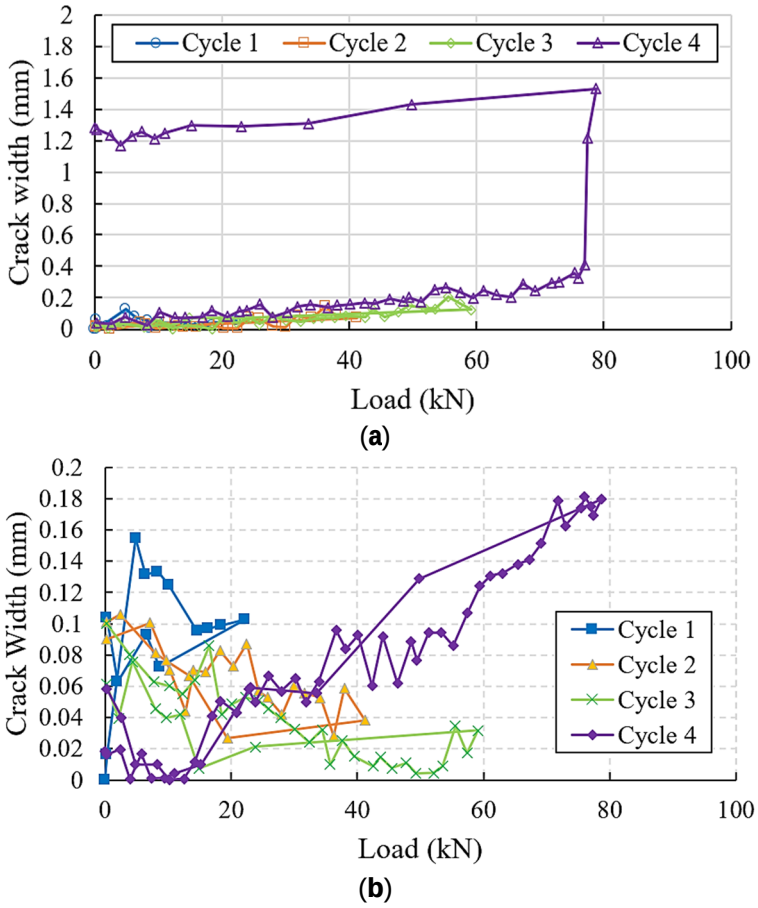


Figure 27. Crack propagation on RC Beam 2 due to: (**a**) flexural crack, and (**b**) flexural–shear crack.

Figure 27b illustrates the propagation of crack number 4 in Beam 2 for each loading cycle. Initially, at the maximum load of the first cycle, the crack width measures 0.103 mm, increasing slightly to 0.104 mm upon unloading. During the second cycle, the crack width shows a tendency to decrease during loading and then increases upon unloading. At the maximum load of the second cycle, the crack width measures 0.038 mm, increasing to 0.101 mm after unloading. Similarly, in the third cycle, the crack width decreases during loading and then increases upon unloading. At the maximum load of the third cycle, the crack width is 0.032 mm, decreasing to 0.062 mm upon unloading. In the fourth cycle, the crack width initially decreases and then continues to increase until the beam reaches the peak of the elastic phase, where it measures 0.174 mm. The crack width increases marginally as the beam enters the plastic phase, reaching a maximum of 0.180 mm. Upon unloading, the crack width decreases to 0.058 mm.

3.6.3. Crack Propagation of RC Beam 3

Figure 28 shows the crack locations observed in RC Beam 3. An analysis will be conducted on flexural crack number 2 in the B–C region of RC Beam 3, due to pure bending. Furthermore, the diagonal flexural–shear crack number 4 in the C–D region will also be analyzed.

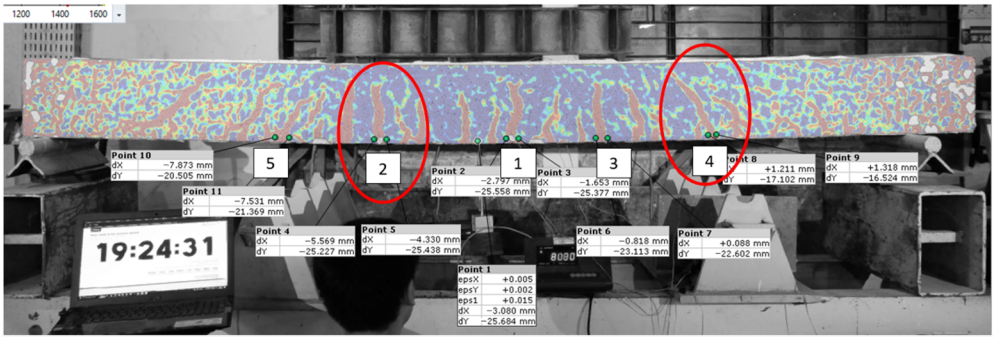


Figure 28. Crack observation points on RC Beam 3: three largest cracks in the B–C area (number 1, 2, and 3) and two largest cracks in both the A–B and C–D areas (number 4 and 5).

In Figure 29a, the propagation of crack number 2 in RC Beam 3 is illustrated for each loading cycle. Initially, at the maximum load of the first cycle, crack number 2 exhibits a width of 0.140 mm, reducing to 0.134 mm upon unloading. During the second cycle, the crack width increases during loading. At the maximum load of the second cycle, it reaches 0.265 mm, subsequently decreasing to 0.124 mm upon unloading. Similarly, during the third cycle, the crack width expands under loading conditions. At the maximum load of the third cycle, it measures 0.312 mm, diminishing to 0.116 mm upon unloading. Moving to the fourth cycle, the crack width continues to enlarge until the beam reaches the peak of the elastic phase, measuring 0.424 mm. Subsequently, the crack width significantly increases as the beam undergoes plastic deformation, reaching a maximum of 1.480 mm during the plastic phase. Upon load release, the crack width decreases to 1.230 mm.

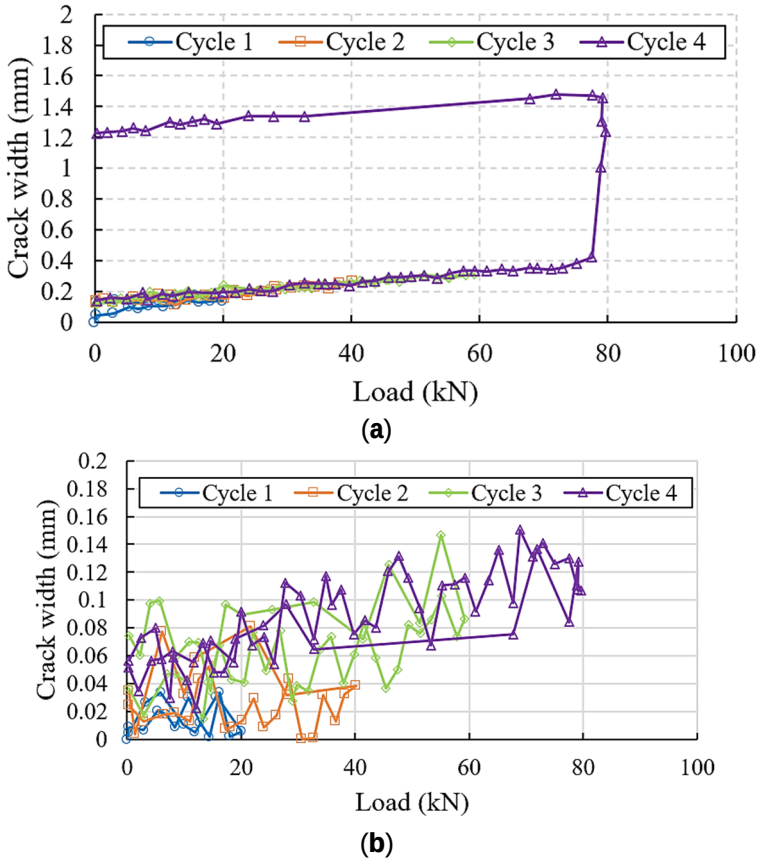


Figure 29. Crack propagation on RC Beam 3 due to: (**a**) flexural crack, and (**b**) flexural–shear crack.

Figure 29b illustrates the propagation of crack number 4 in RC Beam 3 for each loading cycle. Initially, at the maximum load of the first cycle, crack number 4 exhibits a width of 0.006 mm, decreasing to 0.004 mm upon unloading. During the second cycle, the crack width initially decreases and then increases as the loading progresses. At the maximum load of the second cycle, it measures 0.038 mm, decreasing to 0.035 mm upon unloading. Similarly, in the third cycle, the crack width follows a pattern of initial decrease and subsequent increase with loading. At the maximum load of the third cycle, it reaches 0.087 mm, decreasing to 0.075 mm upon unloading. In the fourth cycle, the crack width initially decreases and then continues to increase until the beam reaches the peak of the elastic phase, measuring 0.130 mm. The crack width increases marginally as the beam enters the plastic phase, reaching a maximum of 0.137 mm. Upon unloading, the crack width decreases to 0.052 mm.

Based on the DIC results of RC beams, crack widths due to pure bending tend to have larger values under loading compared to those due to bending–shear. The phenomenon of crack reclosure is observed based in the analyzed crack propagation, wherein crack widths increase with applied load and then decrease upon load release.

4. Results and Discussion of Numerical Study

Numerical modeling of multi-fiber beams in CAST3M is based on experimental beam testing that has been conducted. The modeling scenario to be analyzed is the deflection at the midpoint of the RC Beam 2 due to semi-cyclic loading. The mechanical behavior model used in this study follows the model used by Nurjulita [52], which is the Mazars concrete material model and Elastoplastic steel model.

4.1. Calibration of Numerical Parameters

Calibration of the cube model is done by comparing the modeling results of the cube using solid elements with DIC testing from previous research [21] due to uniaxial compression loads. Then, the model response to uniaxial tensile loads is also generated. The magnitude of concrete and steel material parameters are presented in Tables 7 and 8. The compressive strength, density, and elastic modulus of concrete are obtained from DIC testing results of previous research on FNS concrete [21]. The tensile strength is obtained from previous tensile testing. The Poisson's ratio value is assumed to be 0.2, similar to normal concrete. The parameters KTR0, ACOM, BCOM, ATRA, BTRA, and BETA need to be determined to achieve model response values that align with experimental testing results. The yield strength of reinforcing steel is obtained from tensile testing of the steel reinforcement in the laboratory. The magnitudes of elastic modulus, Poisson's ratio, density, and strain hardening modulus of steel are assumed to be similar to standard steel properties.

Table 7. Mazars concrete parameter.

Items	Parameters	Unit
fc′	43.3×10^6	Pa
fct	2.42×10^6	Pa
E	$16{,}797 \times 10^6$	Pa
Poisson's Ratio (v)	0.2	
Density	2350	kg/m^3
KTR0	0.7×10^{-4}	
ACOM	1.1	
BCOM	570	
ATRA	0.7	
BTRA	20,000	
BETA	1.05	

Table 8. Elastoplastic steel parameters.

Item	Parameters	Unit
E	200×10^9	Pa
Poisson's Ratio	0.3	
Density	7800	kg/m^3
fy	451.62×10^6	Pa
Modulus Strain Hardening	2.5	GPa

The cube model was calibrated (Figure 30), the numerical parameters of this model are then applied to the beam model for further validation against experimental results.

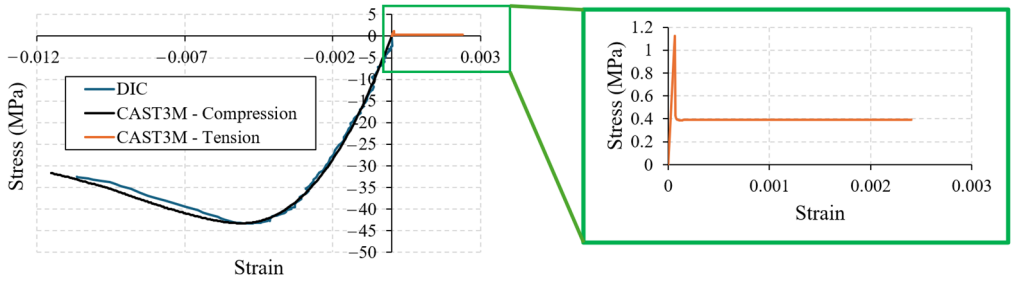


Figure 30. Calibration of numerical parameter: CAST3M vs. DIC method.

4.2. Validation of RC Beam under Monotonic Loading

The validation involves comparing laboratory test results with CAST3M modeling results. Specifically, the comparison focuses on deflection at the beam's midpoint during semi-cyclic loading. These deflection values are converted into monotonic deflection by disregarding deflection during load release cycles. These deflection results are then compared with the modeling results of the Timoshenko multi-fiber elements under monotonic loading (Figure 31).

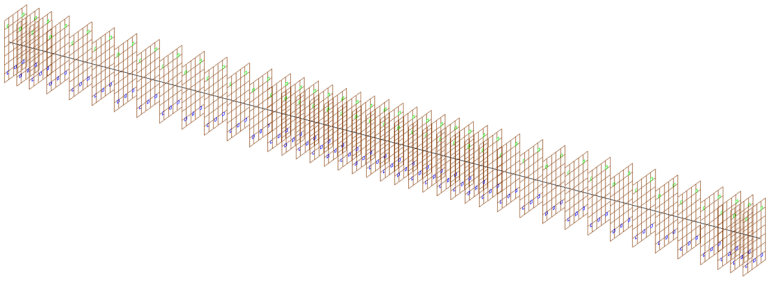


Figure 31. The 3D geometric model of the multi-fiber Timoshenko elements in CAST3M.

The results of the beam model response using cube parameters are presented in Figure 32. It is evident that the model response does not closely align the beam test results (LVDT vs. numerical model 1). To address this issue, additional numerical parameter studies are conducted. Using numerical model parameters 2 (modified Mazars) as shown in Table 9, the experimental results and the numerical model 2 curves closely align, as shown in Figure 32. Therefore, the numerical model 2 parameters (modified Mazars) will be used in modeling RC beams with the substitution of 50% nickel slag fine aggregate under semi-cyclic loading.

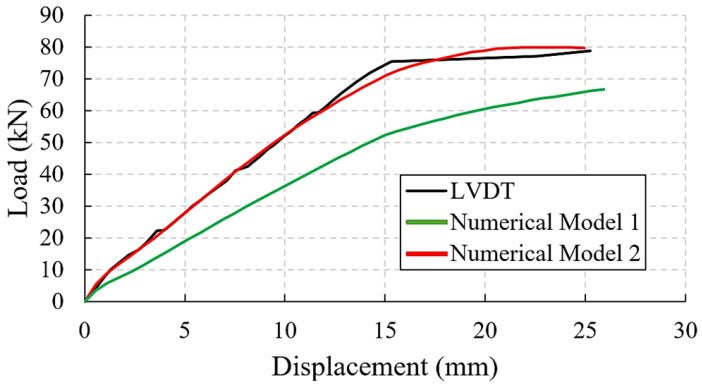


Figure 32. Validation between experimental and numerical results of RC beam under monotonic loading.

Table 9. Modified Mazars concrete parameter.

Items	Parameters	Unit
fc′	43.299×10^6	Pa
E	29.513×10^9	Pa
Poisson's Ratio (v)	0.2	
Density	2350	kg/m^3
KTR0	0.7×10^{-4}	
ACOM	1.5	
BCOM	1400	
ATRA	0.7	
BTRA	20,000	
BETA	1.05	

4.3. Validation of RC Beam under Semi-Cyclic Loading

Figure 33 provides an illustration of the stress pattern in the X-direction under maximum loading conditions. The red-colored areas between the two loading points represent areas under tension, while the blue-colored areas represent areas under compression. These conditions align with the theory where, when the beam is loaded from the top, the upper fibers of the beam experience tension and the lower fibers experience compression. Furthermore, the darker shades of blue and red indicate maximum values in the upper and lower fibers, respectively. The darker shades of blue and red indicate maximum stress concentrations in the upper and lower fibers, respectively. Based on these findings, it is predicted that significant cracking will occur between the two load points, consistent with the experimental test results (B–C area).

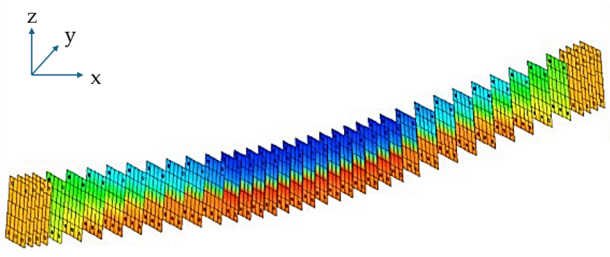


Figure 33. Stress distribution at the maximum load condition during semi-cyclic loading.

Comparison of deflection results at the midpoint of the beam between CAST3M modeling and experimental testing is presented in Figure 34. In the first cycle (Figure 34a), the model deflection closely resembles the experimental results until reaching the maximum load. After unloading, the model deflection could not exhibit residual deflection in the beam, where the model beam deflection appears to return to 0. The model deflection at the end of the cycle is adjusted to have residual deflection like the test results. However,

the modeled residual deflection does not occur at a load of 0. This limitation is due to the Mazars concrete model, where the modeled concrete remains entirely elastic and lacks unrecoverable deformation [39,45], theoretically resulting in no residual deflection if the beam is still in the elastic phase.

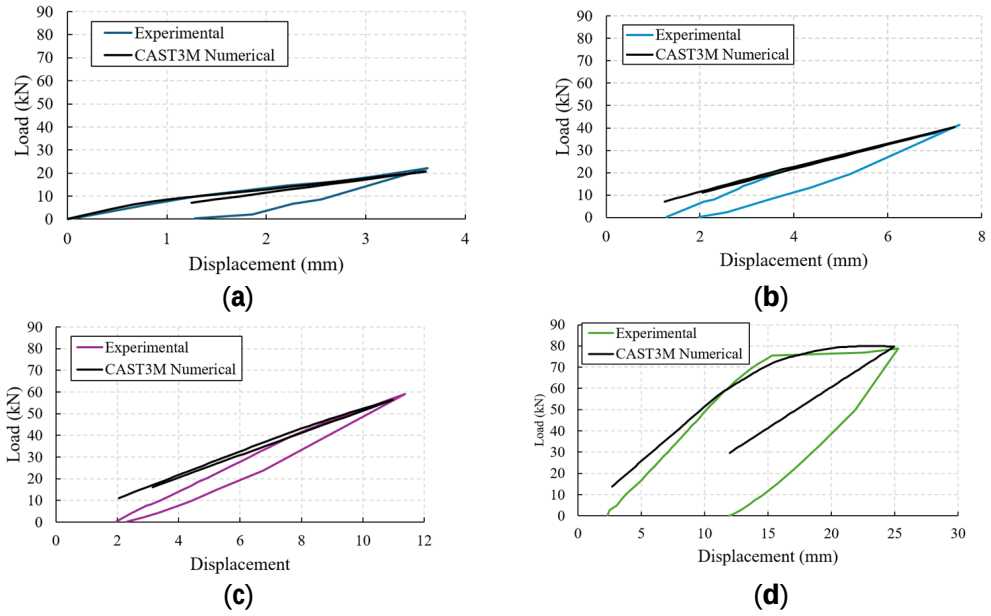


Figure 34. Validation between experimental and numerical results of RC beam under semi-cyclic loading: (**a**) Cycle 1, (**b**) Cycle 2, (**c**) Cycle 3, and (**d**) Cycle 4.

In the second (Figure 34b) and third cycles (Figure 34c), the model deflection starts from a "residual" deflection and then gradually resembles the experimental results until the maximum load of those cycles. The slope of the model curve appears flatter due to the different starting points of the loading cycle between the numerical model and the experiment.

In the fourth cycle (Figure 34d), the semi-plastic phase deflection in the beam is not as smooth as in the model. However, the largest deflection in the plastic phase of both the model and the experiment appears to be similar. Nevertheless, after unloading the beam, the residual deflection of the model does not reach 0 kN, unlike the experimental results. Nonetheless, upon closer inspection, the unloading line in the numerical model projects a residual deflection or deformation of 5 mm at the 0 kN point, indicating that the beam model has reached its plastic phase.

It is evident that the multi-fiber Timoshenko model using modified Mazars concrete damage and Elastoplastic steel provides reasonably good deflection results during the loading phase. However, there are limitations to the model in producing deflection results consistent with the experimental results during the unloading phase. Alternative advanced constitutive models for concrete materials, such as the modified Mazars damage model incorporating higher-order beam theories based on the Carrera Unified Formulation [53], could be investigated to refine numerical simulations of residual displacements under semi-cyclic loading conditions.

5. Conclusions

This research contributes to civil engineering by showcasing the potential of FNS in sustainable concrete production and providing insights into the structural behavior of RC beams under semi-cyclic loading, supported by experimental testing and numerical validation. Key findings from the study of RC beams with 50% FNS fine aggregate substitution (FNS RC Beams) include:

- FNS RC beams demonstrated robust performance under semi-cyclic loading, exceeding theoretical capacity calculations.
- The study compared load–displacement curves from LVDT and DIC methods, finding DIC consistently showed smaller displacements, especially upon load release.
- DIC effectively captured material response, surface deformations, and crack patterns, underscoring its utility in structural assessments and long-term durability evaluations.
- The crack evolution in the beams initially showed elastic behavior with crack propagation under bending moments. With increased loads, plastic deformation occurred, characterized by larger, sustained cracks and residual strains.
- Cracks in the B–C area primarily experienced pure bending, while A–B and C–D regions exhibited flexural–shear behavior, influencing crack widths and propagation patterns.
- All RC beams showed resilient behavior, with deflections returning close to initial states post-unloading, indicating retained elastic properties due to steel reinforcement. Stiffness varied during loading, reflective of localized crack initiation.
- FNS RC beams demonstrated higher stiffness compared to normal and OPS RC beams, with lower maximum displacements but higher residual displacements, indicating potential long-term deformability.
- The CAST3M model, using modified Mazars concrete damage and elastoplastic steel models, showed reasonable agreement with experimental deflection data during loading phases. However, it struggled with residual deflections during unloading, suggesting the need for model enhancements to better capture irreversible deformations.

In conclusion, the research highlights the viability of FNS as a sustainable alternative in reinforced concrete structures, balancing performance with environmental goals. FNS RC beams exhibited comparable mechanical properties to normal RC beams, supporting their future application in concrete construction. The study's insights into surface deformation and crack propagation are crucial for advancing structural engineering practices towards safer, more durable, and sustainable concrete structures.

Several limitations and future research considerations should be noted. Firstly, specific constitutive models such as the Mazars concrete damage model may not fully capture all nuances of concrete behavior. Future studies could explore advanced models or hybrid approaches integrating higher-order beam theories to improve accuracy in predicting residual displacements under semi-cyclic loading. Secondly, the experimental validation was limited to specific loading conditions and types of structures. Future research should expand experimental validations to include other types of structures (e.g., beam-column joints) and consider environmental exposures to enhance applicability. Investigating the long-term durability of FNS RC beams, including effects such as corrosion, is crucial for assessing practical feasibility and advantages in real-world applications.

Author Contributions: Conceptualization, J.S. and N.H.; methodology, J.S., E.E. and N.H.; software, E.E.; validation, J.S., E.E., E.V. and N.H.; formal analysis, J.S., E.E. and N.H.; investigation, J.S.; resources, J.S. and E.E.; data curation, J.S., E.E., N.H. and S.A.; writing—original draft preparation, J.S. and E.E.; writing—review and editing, J.S. and E.V.; visualization, J.S. and E.E.; supervision, J.S., S.A. and N.H.; project administration, E.E.; funding acquisition, J.S. All authors have read and agreed to the published version of the manuscript.

Funding: The research was funded by the Directorate of Research and Development, Universitas Indonesia, under Hibah PUTI Q2 (Grant No. NKB-819/UN2.RST/HKP.05.00/2023).

Data Availability Statement: The data presented in this study are available on request from the corresponding author.

Conflicts of Interest: The authors declare no conflicts of interest.

References

1. Chow, R.K.K.; Yip, S.W.S.; Kwan, A.K.H. Processing Crushed Rock Fine to Produce Manufactured Sand for Improving overall Performance of Concrete. *HKIE Trans.* **2013**, *20*, 240–249. [CrossRef]

2. Mundra, S.; Sindhi, P.R.; Chandwani, V.; Nagar, R.; Agrawal, V. Crushed Rock Sand—An Economical and Ecological Alternative to Natural Sand to Optimize Concrete Mix. *Perspect. Sci.* **2016**, *8*, 345–347. [CrossRef]
3. Sankh, A.C.; Biradar, P.M.; Naghathan, S.J. Recent Trends in Replacement of Natural Sand with Different Alternatives. *IOSR J. Mech. Civ. Eng.* **2014**, 59–66. Available online: https://api.semanticscholar.org/CorpusID:54778030 (accessed on 6 July 2024).
4. El Machi, A.; El Berdai, Y.; Mabroum, S.; Safhi, A.e.M.; Taha, Y.; Benzaazoua, M.; Hakkou, R. Recycling of Mine Wastes in the Concrete Industry: A Review. *Buildings* **2024**, *14*, 1508. [CrossRef]
5. Xie, Y.; Far, H.; Mortazavi, M.; El-Sherbeeny, A.M. Improving the Mechanical Properties of Concrete Mixtures by Shape Memory Alloy Fibers and Silica Fume. *Buildings* **2024**, *14*, 1709. [CrossRef]
6. Fernandes, F.A.d.S.; Fernandes, T.F.d.S.; Rossignolo, J.A. Production of Glass Foam in a Microwave Oven Using Agro-Industrial Waste as Raw Material. *Buildings* **2024**, *14*, 1643. [CrossRef]
7. Gandhi, S.; Roji, S.S.S.; Motta, M.; Nalawade, R.R.D.; Khan, M.A.; Palanisamy, S. Analysis of Potential Incorporation of Waste into Asphalt Pavements. *Mater. Today Proc.* 2024, *in press*. [CrossRef]
8. Bahoria, B.V.; Ranjith, A.; Laxmaiah, G.; Raj, S.S.; Padhi, M.R.; Palanisamy, S. Verification of the Mechanical Behavior of Concrete with Partial Replacement of the Fiber Resulting from Tire Retreading. *Mater. Today Proc.* 2024, *in press*. [CrossRef]
9. Santhosh, N.; Selvam, S.; Reghu, R.; Sundaran, J.; Mathew, B.C.; Palanisamy, S. Mechanical Properties Studies on Rubber Composites Reinforced with Acacia Caesia Fibre. *Mater. Today Proc.* **2023**, *72*, 3172–3176. [CrossRef]
10. Al-Jabri, K.S.; Al-Saidy, A.H.; Taha, R. Effect of Copper Slag as Fine Aggregate on the Properties of Cement Mortars and Concrete. *Constr. Build. Mater.* **2011**, *25*, 933–938. [CrossRef]
11. Valcuende, M.; Benito, F.; Minano, I. Shrinkage of Self-compacting Concrete Made with Blast Furnace Slag as Fine Aggregate. *Constr. Build. Mater.* **2015**, *76*, 1–9. [CrossRef]
12. Koganti, A.P.; Hemanthraja, K.; Sajja, S. Replacement of Fine Aggregate by using Recyclable Materials in Paving Blocks. *IOP Conf. Ser. Mater. Sci. Eng.* **2017**, *225*, 012157. [CrossRef]
13. Guo, Y.; Xie, J.; Zheng, W.; Li, J. Effects of Steel Slag as Fine Aggregate on Static and Impact Behaviours of Concrete. *Constr. Build. Mater.* **2018**, *192*, 194–201. [CrossRef]
14. Surangi, M.L.C.; Julnipitawong, P.; Tangtermsirikul, S.; Ohgi, Y.; Ishii, Y. Using Fly Ash as a Partial Replacement for Fine Aggregate in Concrete Properties under Different Curing Temperatures. *ASEAN Eng. J.* **2020**, *10*, 35–49. [CrossRef]
15. Sugiri, S. Persamaan Korelasi Sifat Mekanik Beton Mutu Tinggi dengan Agregat Alami dan Slag Nikel. *J. Tek. Sipil* **2007**, *14*, 27–40. [CrossRef]
16. Saha, A.K.; Sarker, P.K. Sustainable Use of Ferronickel Slag Fine Aggregate and Fly Ash in Structural Concrete: Mechanical Properties and Leaching Study. *J. Clean. Prod.* **2017**, *162*, 438–448. [CrossRef]
17. Wijaya, R. Karakteristik dan Kuat Tekan Mortar Dengan Subtitusi Terak Nikel Sebagai Agregat Halus. Master's Thesis, Universitas Indonesia, Jawa Barat, Indonesia, 2021. (In Bahasa Language)
18. Wijaya, R.; Astutiningsih, S. Studi Literatur Potensi Pemanfaatan Terak Nikel (Slag Nikel) sebagai Agregat pada Mortar dan Beton. *Bentang* **2021**, *9*, 93–100. [CrossRef]
19. Mustika, W.; Salain, I.M.A.K.; Sudarsana, I.K. Penggunaan Terak Nikel Sebagai Agregat Dalam Campuran Beton. *Spektran* **2016**, *4*, 36–45. [CrossRef]
20. Edwin, R.S.; Ngii, E.; Talanipa, R.; Masud, F.; Sriyani, R. Effect of Nickel Slag as a Sand Replacement in Strength and Workability of Concrete. *IOP Conf. Ser. Mater. Sci. Eng.* **2019**, *615*, 012014. [CrossRef]
21. Ernawan, E.; Sjah, J.; Handika, N.; Astutiningsih, S.; Vincens, E. Mechanical Properties of Concrete Containing Ferronickel Slag as Fine Aggregate Substitute Using Digital Image Correlation Analysis. *Buildings* **2023**, *13*, 1463. [CrossRef]
22. Manuel, I. Compressive Strength Evaluation of Concrete with Nickle Slag and M-Sand as Fine Aggregate Substitution Using Digital Image Correlation and Ultrasonic Pulse Velocity. Bachelor's Thesis, Universitas Indonesia, Jawa Barat, Indonesia, 2023. (In Bahasa Language)
23. Saha, A.K.; Sarker, P.K.; Majhi, S. Effect of Elevated Temperatures on Concrete Incorporating Ferronickel Slag as Fine Aggregate. *Fire Mater.* **2019**, *43*, 8–21. [CrossRef]
24. Saha, A.K.; Sarker, P.K. Durability Characteristics of Concrete using Ferronickel Slag Fine Aggregate and Fly Ash. *Mag. Concr. Res.* **2018**, *70*, 865–874. [CrossRef]
25. Nguyen, Q.D.; Castel, A.; Kim, T.; Khan, M.S.H. Performance of Fly Ash Concrete with Ferronickel Slag Fine Aggregate against Alkali-silica Reaction and Chloride Diffusion. *Cem. Concr. Res.* **2021**, *139*, 106265. [CrossRef]
26. Bao, J.; Yu, Z.; Wang, L.; Zhang, P.; Wan, X.; Gao, S.; Zhao, T. Application of Ferronickel Slag as Fine Aggregate in Recycled Aggregate Concrete and the Effects on Transport Properties. *J. Clean. Prod.* **2021**, *304*, 127149. [CrossRef]
27. U.S. Geological Survey. *Mineral Commodity Summaries*; U.S. Geological Survey: Reston, VA, USA, 2021.
28. Ministry of Industry of Indonesia, Kemenperin Angkat Potensi Slag Nikel Jadi Bahan Baku Industri. 2020. Available online: https://kemenperin.go.id/artikel/21806/Kemenperin-Angkat-Potensi-Slag-Nikel-Jadi-Bahan-Baku-Industri (accessed on 15 May 2021). (In Bahasa Language).
29. Raju, S.; Rathinam, J.; Dharmar, B.; Rekha, S.; Avudaiappan, S.; Amran, M.; Usanova, K.I.; Fediuk, R.; Guindos, P.; Ramamoorthy, R.V. Cyclically Loaded Copper Slag Admixed Reinforced Concrete Beams with Cement Partially Replaced with Fly Ash. *Materials* **2022**, *15*, 3101. [CrossRef] [PubMed]

30. Murad, Y.; Abu-Haniyi, Y.; Alkaraki, A.; Hamadeh, Z. An Experimental on Cylic Behaviour of Reinforced Concrete Connections using Waste Materials as Cement Partial Replacement. *Can. J. Civ. Eng.* **2019**, *46*, 522–533. [CrossRef]
31. Ramasamy, G.; Kannan, S.P.R. Flexural Behaviour of High-performance Concrete Beams under Cyclic Loading Conditions. *J. Eng. Res.* **2022**, 1–12. [CrossRef]
32. Bhoopathy, V.; Subramanian, S.S. The Way Forward to Sustain Environmental Quality through Sustainable Sand Mining and the Use of Manufactured Sand as an Alternative to Natural Sand. *Environ. Sci. Pollut. Res.* **2022**, *29*, 30793–30801. [CrossRef] [PubMed]
33. Elavenil, D.S.; Bhoopathy, V. Manufactured Sand, A Solution and An Alternative to River Sand in Concrete Manufacturing. *Int. J. Civ. Eng. Res. Dev.* **2013**, *3*, 1–7.
34. *ASTM C39/C39M*; Standard Test Method for Compressive Strength of Cylindrical Concrete Specimens. ASTM International: West Conshohocken, PA, USA, 2023. [CrossRef]
35. *ASTM C496/C496M*; Standard Test Method for Splitting Tensile Strength of Cylindrical Concrete Specimens. ASTM International: West Conshohocken, PA, USA, 2017. [CrossRef]
36. *ASTM C597*; Standard Test Method for Ultrasonic Pulse Velocity through Concrete. ASTM International: West Conshohocken, PA, USA, 2022. [CrossRef]
37. Daniel. Daniel. Studi Eksperimen Karakteristik Dinamik Balok Beton dengan Agregat Daur Ulang (RAC—Recycled Aggregate Concrete) di Bawah Pembebanan Semi-Siklik. Bachelor's Thesis, Universitas Indonesia, Jawa Barat, Indonesia, 2021. (In Bahasa Language)
38. Handika, N. Multi-Cracking of Reinforced Concrete Structures: Image Correlation Analysis and Modelling. Ph.D. Thesis, INSA de Toulouse, Toulouse, France, 2017.
39. Hongsen, K.; Melhan, M.; Handika, N.; Sentosa, B.O.B. Parameterization of Oil Palm Shell Concrete on Numerical Damage Model Based on Laboratory Experiment Using Digital Image Correlation. *J. Phys. Conf. Ser.* **2021**, *1858*, 012029. [CrossRef]
40. Gasti, M.D. Studi Eksperimental Digital Image Correlation dan Karakteristik Dinamik Studi Kasus Balok Beton Bertulang dengan Agregat Normal dan Cangkang Kelapa Sawit. Bachelor's Thesis, Universitas Indonesia, Jawa Barat, Indonesia, 2022. (In Bahasa Language)
41. Sjah, J.; Handika, N.; Adnanta, N.K.; Nurhakim, M.Y.; Vincens, E. Digital Image Correlation for the Determination of Mechanical Properties of Concrete with Modified Expanded Polystyrene. *Int. J. Technol.* **2024**, *15*, 394–403. [CrossRef]
42. Sentosa, B.O.B. Caractérisation d'éléments Structurels en Béton Armé par Mesures Dynamiques. Ph.D. Thesis, Université Grenoble Alpes, Saint-Martin-d'Hères, France, 2018. Available online: https://tel.archives-ouvertes.fr/tel-02134313v2 (accessed on 3 June 2024).
43. Bitar, I.; Grange, S.; Kotronis, P.; Benkemoun, N. A Comparison of Displacement-based Timoshenko Multi-fibre Beams Finite Element Formulations and Elasto-plastic Applications. *Eur. J. Environ. Civ. Eng.* **2018**, *22*, 464–490. [CrossRef]
44. Mazars, J. A Description of Micro and Macroscale Damage of Concrete Structure. *Eng. Fract. Mech.* **1986**, *25*, 729–737. [CrossRef]
45. Mazars, J.; Hamon, F.; Grange, S. *A New 3D Damage Model for Concrete under Monotonic, Cyclic, and Dynamic Loading*; Internal Report 3SR 2013/12; Lab. 3SR: Grenoble, France, 2015.
46. Pijaudier-Cabot, G.; Mazars, J. Damage Models for Concrete. In *Handbook of Materials Behavior Models*; Elsevier: Amsterdam, The Netherlands, 2001; pp. 500–512. [CrossRef]
47. Handika, N.; Sentosa, B.O.B.; Gasti, M.D. Deflection Measurement and Crack Propagation Observation using Contactless Device Digital Image Correlation (DIC) on Concrete Beam. In Proceedings of the Annual Seminar of HAKI (Construction Experts Association), Borobudur Hotel Jakarta, Indonesia, 23–25 August 2022; pp. 1–15.
48. Handika, N.; Astutiningsih, S.; Sentosa, B.O.B.; Gasti, M.D. Crack Propagation Observation using Digital Image Correlation (DIC) on Oil Palm Shell (OPS) Reinforced Concrete Beam. *J. Tek. Sipil Dan Lingkung.* **2024**, *9*, 1–10.
49. Montero, W.; Farag, R.; Diaz, V.; Ramirez, M.B.; Boada, B. Uncertainties Associated with Strain-Measuring Systems Using Resistance Strain Gauges. *J. Strain Anal. Eng. Des.* **2011**, *46*, 1–13. [CrossRef]
50. Neville, A.M.; Brooks, J.J. *Concrete Technology*, 2nd ed.; Prentice Hall: Harlow, UK, 2010; ISBN 978-0-273-73219-8.
51. Timoshenko, S.P.; Gere, J.M. Theory of Elastic Stability, 2nd ed.McGraw-Hill International Book Company: New York, NY, USA, 2009; ISBN 0-07-Y85821-7.
52. Nurjulita, D. Studi Permodelan Numerik Balok Beton Cangkang Kelapa Sawit dengan Elemen Multi-Fiber Timoshenko dengan Menggunakan Software CAST3M 2021. Bachelor's Thesis, Universitas Indonesia, Jawa Barat, Indonesia, 2021. (In Bahasa Language)
53. Shen, J.; Arruda, M.R.T.; Pagani, A. Concrete Damage Analysis Based on Higher-order Beam Theories using Fracture Energy Regularization. *Mech. Adv. Mater. Struct.* **2023**, *30*, 4582–4596. [CrossRef]

Disclaimer/Publisher's Note: The statements, opinions and data contained in all publications are solely those of the individual author(s) and contributor(s) and not of MDPI and/or the editor(s). MDPI and/or the editor(s) disclaim responsibility for any injury to people or property resulting from any ideas, methods, instructions or products referred to in the content.